Targeted Computational Design of an Interleukin-7 Superkine with Enhanced Folding Efficiency and Immunotherapeutic Efficacy

See-Khai Lim[1] , Wen-Ching Lin[1] , Yi-Chung Pan[1] , Sin-Wei Huang[1], Yao-An Yu[1], Cheng-Hung Chang[1], Che-Ming Jack Hu[1]*, Chung-Yuan Mou[2]*, and Kurt Yun Mou[†]

[1] Institute of Biomedical Sciences, Academia Sinica, Taipei, 11529, Taiwan.

[2] Department of Chemistry, National Taiwan University, Taipei, 106319, Taiwan.

* E-mail: chu@ibms.sinica.edu.tw and cymou@ntu.edu.tw

†The author passed away on August 28th, 2023.

Abstract

Interleukin-7 (IL-7) plays a central role in maintaining T cell development and immune homeostasis, and enhancing the cytokine's immune-stimulatory functionality has broad therapeutic implications against various oncological malignancies. Herein, we show a computationally designed IL7 superkine, Neo-7, which exhibits enhanced folding efficiency and superior binding affinity to its cognate receptors. To streamline the protein candidate prediction and validation process, the loop region of IL7 was strategically targeted for redesign while most of the receptor-interacting regions were preserved. Leveraging advanced computational tools such as AlphaFold2, we show loop remodeling to rectify structural irregularities that allows for iterative stabilization of protein backbone and leads to identification of beneficial mutations conducive to receptor engagement. Neo-7 superkine shows improved thermostability and production yield, and it exhibits heightened immune-stimulatory and

anticancer effect. These findings underscore the utility of a targeted computational approach for de novo cytokine development.

Introduction

Clinical success with immune checkpoint inhibitors (ICIs) and immunogenic cell death (ICD) inducers has invigorated developmental efforts on immunotherapeutic strategies that strengthen the body's immune system against oncological malignancies [1-4] [4, 5]. The promise of durable tumor suppression by immunotherapeutic approaches has rekindled enthusiasm towards cytokine therapies, which can enhance immune responses and promote a more effective attack on cancer cells by directly stimulating the proliferation and activation of various immune cell types [6-8]. Cytokine-mediated immune cells activation can override the negative feedback mechanisms and bolster immune cell stimulation, allowing for broad-spectrum tumor suppression and synergistic actions with ICIs and ICD inducers [9, 10]. However, traditional cytokine therapies have been hampered by challenges such as short half-lives, poor pharmacokinetics, and significant toxicity at therapeutic doses [7, 11]. These issues have hindered the broader application of cytokines in cancer treatment despite their potential benefits. For instance, IL-2, one of the first cytokines identified with potent anti-cancer properties, is limited by severe adverse effects, restricting its maximum tolerated dose (MTD) to 37 μg/kg, which in turn limits its efficacy [12]. Similar toxicity concerns exist for other interleukins, such as IL-12, IL-15, and IL-21, with clinical MTDs of 1.0, 20, and 100 μg/kg, respectively [13-15], thus prompting emerging protein design strategies for cytokine variant development with elevated efficacy profiles.

Advances in computational protein design have opened up new opportunities for cytokine engineering, which enables de novo design of cytokine variants with improved stability, reduced toxicity, and enhanced efficacy. These engineered cytokines can be structurally modified for enhanced engagement with their putative cognate receptors, leading to enhanced elevated therapeutic and safety profiles for treatment development. A notable example is the work by Silva et al. (2019), which demonstrated a significant breakthrough in computational protein design [11]. Using the Rosetta protein design suite, they

restructured and redesigned 4-helix bundle mimetics of IL-2 and IL-15 (neo-2/15), resulting in proteins that are more potent and stable both *in vitro* and *in vivo*, with specifically programmed receptor specificity. Although the seminal study showcased the possibility for researcher to design novel protein with computationally idealized structure in its entirety, such approach demands substantial computing resources and can generate many non-analogous candidates for validation. We envision that a targeted redesign strategy that focuses on protein domains with manifest folding inefficiency can minimize the resources required for computational protein engineering. In the present work, the targeted computational design strategy is demonstrated through the development of an IL-7 variant.

Interleukin-7 (IL-7) is a member of the common gamma chain (γc) receptor family, which includes cytokines such as IL-2, IL-15, and IL-21 [8, 16, 17]. IL-7 plays a crucial role in the survival, differentiation, and proliferation of immune cells, including T-lymphocytes, B-lymphocytes, and natural killer (NK) cells [6, 18]. *In vitro* studies have shown that IL-7 promotes the survival and homeostatic proliferation of splenocytes by upregulating survival factors like Bcl-2. Preclinical animal studies and clinical trials have demonstrated broader functions, including the induction and maintenance of memory T cells, promotion of T cell homing to lymphoid organs, increased T cell receptor diversity, and enhanced T cell cytotoxicity by the cytokine [6, 18-20]. The first-generation IL-7, known as CYT-107, demonstrated potent immune cell reconstitution in phase 2 clinical trials for HIV patients (for CD4+ T cell restoration) and patients with sepsis-induced lymphopenia [21-23]. However, its anti-cancer efficacy was limited, as it increased immune cell count but did not induce a significant anti-tumor response, likely due to its short half-life (8.7-34.6 hours) [6, 18, 21, 24]. The second-generation IL-7 drug, NT-I7 (efineptakin alfa), uses a hybrid human IgG/IgD Fc domain for half-life extension (T1/2 = 60.8-139.7 hours), which significantly improves its anti-tumor activities. Efineptakin alfa supports the proliferation and survival CD4+ and CD8+ cells in both human and mice showing promising responses in early-phase clinical trials for advanced solid tumors, particularly in combination with immune checkpoint inhibitors [6, 20, 24].

Although much efforts have been devoted to enhance IL-7 pharmacokinetics through protein fusion, no variant or computationally designed mimic has been reported on the cytokine to our knowledge.

From a development perspective, IL-7 is prone to aggregation and requires additional engineering to enhance its solubility and stability. To address these challenges, we herein engineer a novel variant of IL-7, known as Neo-7, with enhanced folding efficiency through targeted computational protein design. By removing redundant loops and redesigning the protein backbone using Rosetta loop remodeling, we reconnected the functional domains in a more efficient and economical structural (In this context, the term efficiency refers to the shortest number of amino acids that is required to connect two receptor-binding or functional helices). Advanced computational tools were employed to ensure that the Neo-7 variant would fold according to the predicted structural models, resulting in a protein with superior folding efficiency and receptor binding affinity. In further experimental studies, Neo-7 demonstrates improved *in vitro* production yield and *in vivo* biological activity, positioning it as a promising candidate for cancer immunotherapy. These advancements underscore the potential of IL-7 and its engineered variants as effective cancer immunotherapies, highlighting the importance of optimizing cytokine properties for clinical application.

Results

Development of a computational pipeline for rational protein design

In redesigning IL-7, we aimed to minimize sequence alterations relative to the wild-type protein. This strategy is based on the understanding that a protein's sequence is closely tied to its structure and function. By preserving the native sequence elements involved in IL-7's biological activity, we sought to maximize the likelihood of producing a successful variant without compromising its original function. We began by examining the crystal structure of IL-7 bound to its receptor, IL7R-α (PDB ID: 3DI2). Loop remodeling was performed using Rosetta's loop remodeling modules, followed by validation with AlphaFold,

employing both single-sequence monomer and multimer models. During the computational design and validation process, each model predicted by either Rosetta or AlphaFold was meticulously inspected using PyMOL and Discovery Studio 4.5. Residues that were found to clash with neighboring amino acids were further refined through mutations using Rosetta's fix backbone modules. The gene sequences of the final designs that successfully passed this computational pre-filtering were then synthesized and cloned into a yeast display vector for subsequent *in vitro* validation (**Figure 1**).

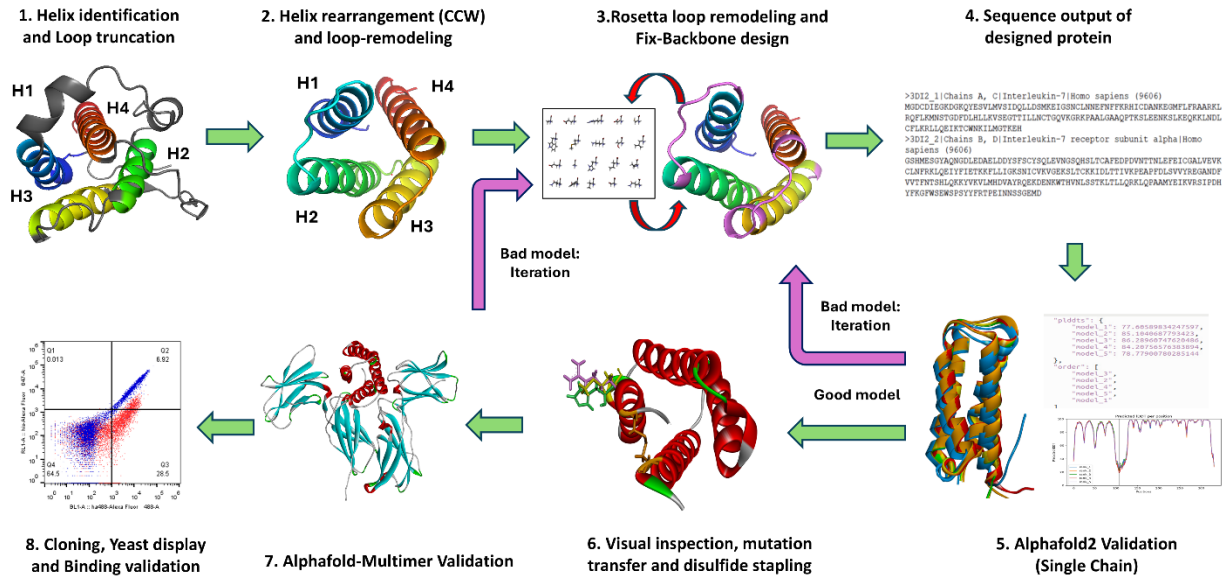

Figure 1. Schematic illustrating the computational pipelines for Neo-7 engineering from wild type IL7 sequence. In general, non-receptor interacting loops were deleted from the WT-IL7 sequence and loops connecting the adjacent helixes were modeled using Rosetta Loop Remodeler and Rosetta fix backbone design function. The sequence of the designed model were extracted and submitted to alphafold (monomer and multimer mode for structure and protein-receptor binding prediction respectively) as an preliminary validation of the Rosetta-remodeled protein. Iterations of the bad models (models that do not fold into the expected structure or models that did not predicted to bind to the receptors) back to the design stage were performed. Models that passed the Alphafold validation proceeded to subsequent *in vitro* assay using yeast display system and flow cytometry to determine their relative binding affinity to IL-7 receptors in comparison to WT-IL7.

The wild-type IL-7 protein forms a 4-helix bundle structure with three inter-helical loops. Upon visually examining its crystal structure in complex with IL-7 receptor alpha (IL7Rα), we noted that the connectivity between each helix is intricate and inefficient (**Figure 2**). In the crystal structure of WT-IL7 complexed with IL-7 receptor alpha, IL-7 is composed of four helices. Helices 1 and 3 are found to interact with IL-7 receptor alpha (IL7R-α), while helices 1 and 4 are predicted to interact with the IL-2 receptor common gamma chain (IL2R-γ) [25]. Helix 2 was observed to serve as a structural support for the helix bundle. However, the connectivity of these helices exhibited complexity and inefficiency. Notably, the loop between helix 1 and 2 spans 29 amino acids (AA), the loop connecting helix 2 and 3 is 6 AA long, and the loop connecting helix 3 and 4 is 35 AA long. We extracted the helices from the PDB structure file and reconnected the helices using Loop Remodel function from the Rosetta suite. The protein was remodeled clockwise in the order of H1>H3>H2>H4. The new loops connecting H1-H3, H3-H2 and H2-H4 are 7, 8 and 5 AA in length respectively. The amino acid sequences of the designed loops were subsequently optimized using Rosetta Fix Backbone design function and validated using Alphafold monomer.

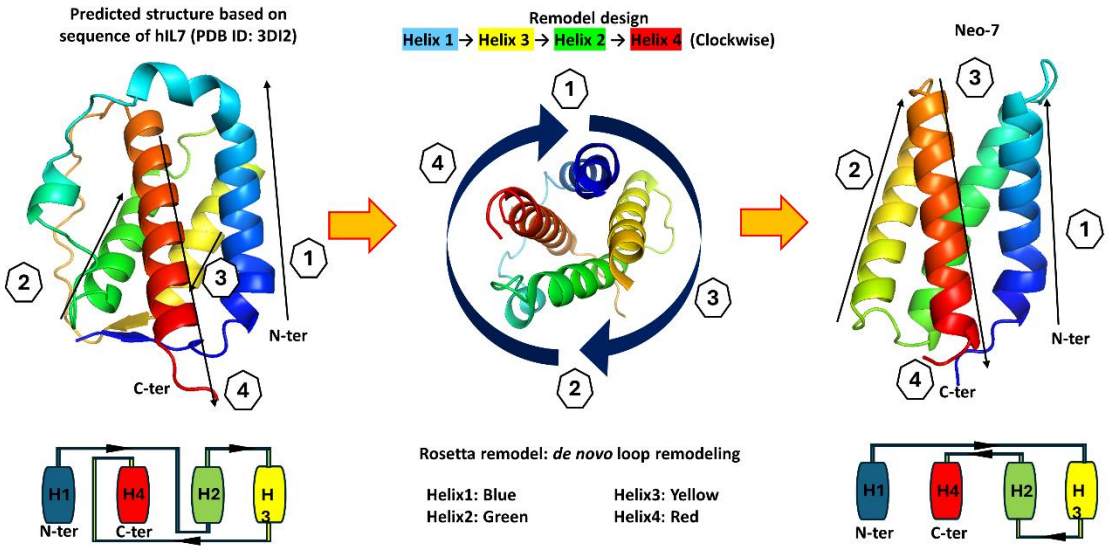

Figure 2. Blueprint of Neo-7 design. Blueprint of the WT-IL7 were shown on the left of the figure. The connectivity of the functioning helixes were connected in a manner that requires extremely long protein loops by design (i.e. helices were not connected to the closest adjacent helixes but to the

opposite helix). Loops that were not interacted with the IL-7 receptors were deleted and the helixes were reconnected in a clockwise manner via new protein linkers connecting to the adjacent helixes. The blueprint of the redesigned protein was shown at the right side of the figure. Protein structures are colored as rainbow (from N-to-C terminus with the order of Blue-Green-Yellow-Red).

Structural Validation of Neo-7 in Alphafold single sequence mode

The synthesized Neo-7 sequence was cloned into a yeast-display vector to assess its expression and binding capability to IL7Rα. Despite the concordance between Rosetta and AlphaFold monomer predictions, no binding was observed between displayed Neo-7 and IL7Rα (**Figure 3C**). Surprisingly, binding to IL2Rγ was detected, suggesting that the displayed protein was partially folded in the yeast display platform. We also postulated that the high similarity between the helices of Neo-7 and WT-IL7 amino acid sequences might lead to sampling bias, leading Alphafold to predict a similar folding of Neo-7 to WT-IL7. To investigate this, we utilized AlphaFold Single Sequence (AlphaFold SS), an online platform capable of performing AlphaFold without relying on a PDB template and MSA database. The resulting structure model from AlphaFold SS indicated misfolding of helix 2 (providing structural support) and helix 3 (binding to IL7Rα) when superimposed onto WT-IL7 helices (**Figure 3A**). However, the helices responsible for binding to the gamma receptor aligned well with the WT template. Subsequently, we addressed the misfolded helices by redesigning their connecting loops (loop 1 and 2) using Rosetta fix backbone design and validated the structures with AlphaFold SS (**Figure 3B**).

Disulfide stapling on Helix 1 and stabilizing mutations are essential for binding of IL-7 and Neo-7 to IL-7 receptor-α.

Since the helices were adapted from the WT-IL7, we hypothesized that those beneficial mutations to stabilize IL-7 or enhance its binding to the cognate receptors should be applicable to our designed

constructs. Prior to the transfer of the beneficial mutations discovered from our previous study (Supplementary Figure S1), we first constructed a multimer-model consisting of Neo-7, murine IL7Rα and the common IL2Rγ receptors using Alphafold Multimer. The resulting model was used as a structure template for Rosetta fix backbone design, which the amino acid variants of the mutants and their wild type counterpart (**Table 1**) were keyed into the Rosetta fix backbone residue files for calculation. Only those mutations that were favored by Rosetta are selected to maximize the stability of the protein and to preserve their theoretical folding in the subsequent *in vitro* yeast display assay.

Table 1. Site-directed mutagenesis residues recommended by Rosetta to improve the folding stability of the Neo-7s.

Residue number	Wild type	Mutant	Remarks	Rosetta's choice
5	K	R	Cytokine-receptor binding interface	R
6	Q	P	Cytokine-receptor binding interface	Q
44	T	I	Cytokine core-surface interface	I
45	I	T	Borderline of cytokine binding interface	T

The Neo-7 design, incorporating Rosetta-favored mutations, demonstrated enhanced protein-display level and binding to IL2Rγ (Figure 3E). However, despite the alignment between computational protein design and prediction programs, weak or insignificant binding of the designed Neo-7 to murine IL7Rα was observed in the yeast display system. A closer examination of the crystal structure of WT-IL7 with IL7Rα revealed a kink on helix 1 is crucial for proper IL7-IL7Rα binding, stabilized by a disulfide bridge on the N-terminus and loop 3 of WT-IL7 (**Figure 3C**). The structure of Neo-7 generated from AlphaFold lacked this kink, possibly due to the absence of the disulfide bridge. To address this, we hypothesized that regenerating the kink through mutations of core amino acids between helix 1 and 4 into cysteine might recapitulate the native kink conformations observed in WT-IL7 (**Figure 3C**). Introducing G4C and L96C mutations into Neo-7 validated this hypothesis, as the resulting disulfide-stapled Neo-7 model predicted

by AlphaFold SS exhibited the reappeared kink on helix 1 (**Figure 3D**). Encouraged by this result, we proceeded to the next stage of *in vitro* evaluation via yeast display using the designed Neo-7.

Meanwhile, to assess the importance of the kink for IL7Rα binding affinity in WT-IL7, we deleted the first 7 amino acids at the N-terminus of WT-IL7 and investigated its binding to murine IL7Rα in the yeast display system. Interestingly, the results (**Figure 3E**) demonstrated that N-terminal truncation fully diminished the binding of IL-7 to IL7Rα. Conversely, for the Neo-7 design, both the disulfide stapling, and Rosetta-favored mutations were found essential for binding to IL7Rα. This indicates that both the helix kink from the disulfide design and core stability conferred by the transferred mutations are required for the generation of a stable and functional Neo-7. Importantly, the enhanced binding affinity towards IL7Rα also led to improved binding towards the common IL2Rγ.

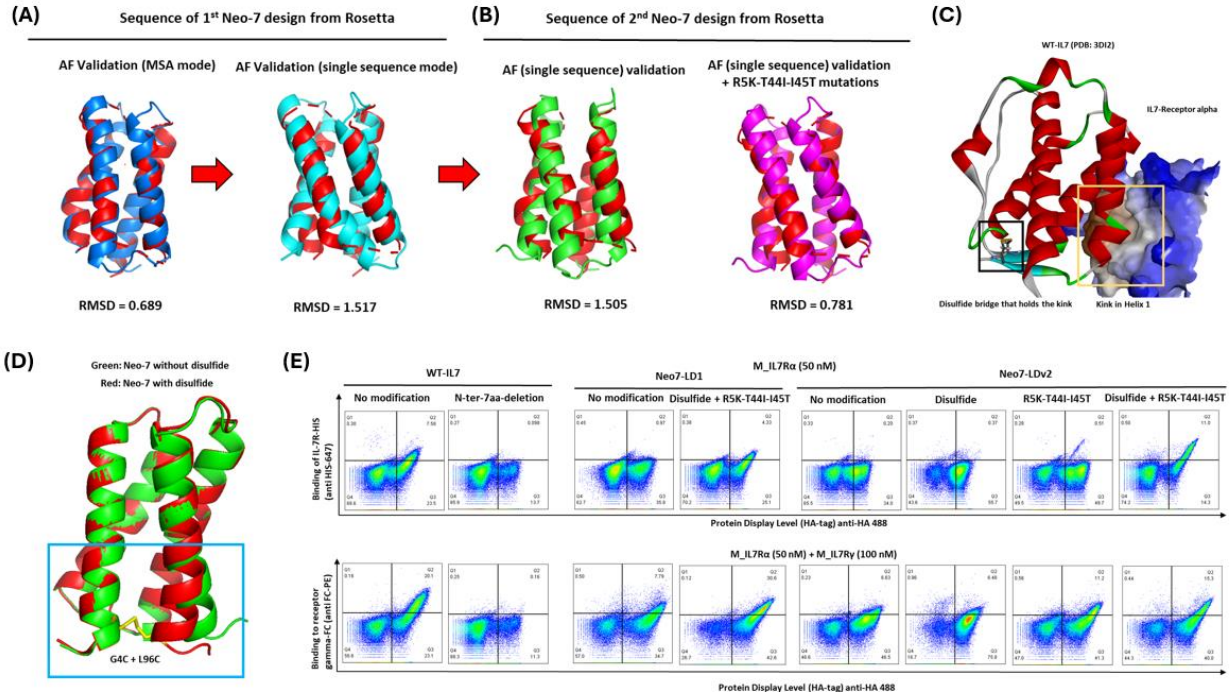

Figure 3. Validation of Neo-7 designs from Rosetta loop remodeling and fix backbone design. (A) Alphafold validation of the first loop design version of neo7 (Neo-7 LDv1) using the default (left) and single sequence mode (right). (B) Alphafold validation of the second loop design version of neo 7 (left; Neo-7 LDv2) and Neo7 LDv2 with mutations (right) favored by Rosetta fix backbone design. (C) Crystal structure of human IL-7 in complexation to human IL-7 receptor alpha (PDB ID = 3DI2). (D)

Superimposition of Neo-7 structures (with or without additional disulfide bridge) predicted by Alphafold. (E) Yeast display and flow cytometry validation of IL-7/Neo-7 bindings towards the IL-7 receptors. The yeast-displayed protein (different redesigned IL-7s) carries a HA-tag while the recombinant IL-7 receptors carries either a HIS tag (IL-7 receptor alpha) or a FC-tag (common-IL-2 family receptor gamma). The signal intensity of the X-axis (confers by the binding of anti-HA mab) correlates with the expression level of the displayed protein while the signal intensity of the Y-axis (confers by the binding of the anti-HIS/anti-FC mab to the recombinant receptors bound to the displayed proteins) correlates with the binding affinity of the displayed proteins towards the IL-7 receptors.

(D) Site-directed mutagenesis residues recommended by Rosetta to improve the folding stability of the Neo-7s.

Transfer of beneficial mutations on the cytokine-receptor binding interface further enhanced the binding of Neo-7 to IL7-Receptor α.

Encouraged by the successful expression of a functional Neo-7 (Neo-7 Loop design 2 with R5K-T44I-I45T mutations, herein referred as Neo-7) design in the yeast display platform, we modeled the structure of Neo-7 in the presence of murine IL7Rα and IL2Rγ. After careful examination of all the mutation points (Figure 4A), we hypothesized that two mutations points might further improve the binding affinity of Neo-7 towards IL7Rα due to the following reasons: (1) Both residues were located closely to a hydrophobic patch of IL7Rα and replacing the polar glutamine and threonine into a more hydrophobic proline or isoleucine are favorable for binding through hydrophobic interactions (2) Proline was disfavored by Rosetta probably due to its specific characteristics as a helix breaker (Table 1). However, after careful inspection of the structure, we observed that proline was located at the starting point of helix 1 that were further stabilized by disulfide stapling and therefore void the concerns on the helix breaking properties of proline under this design. (3) At position 45, threonine is favored by Rosetta in comparison to the wild type isoleucine residue. Such decision might arise from the additional consideration of the

stability of Neo-7 monomer in aqueous solution as an exposed hydrophobic residue in the aqueous environment is energetically unfavorable. However, after comparing the binding conformations of threonine and isoleucine with IL7Rα, we decided that isoleucine was observed to have better shape complementarity that could occupy the hydrophobic pocket at the Neo-7- IL7Rα interface. Subsequently, we constructed the relevant mutants for Neo-7, sampling the effects of mutations located at the Neo-7-IL7Rα interface towards their binding to IL7Rα. Interestingly, the Q6P mutations showed the most prominent enhancements in the yeast display system while T45I mutation showed moderate improvement for IL7Rα. Double mutations of Q6P and T45I further improved the binding affinities of Neo-7 to both IL7Rα and IL2Rγ, suggesting an additive effects of the binding improvement (Figure 4B). Two best variants, Neo-7 with Q6P mutation and Neo-7 with dual mutations (Q6P + T45I) were selected for subsequent *in vitro* bioactivity assay.

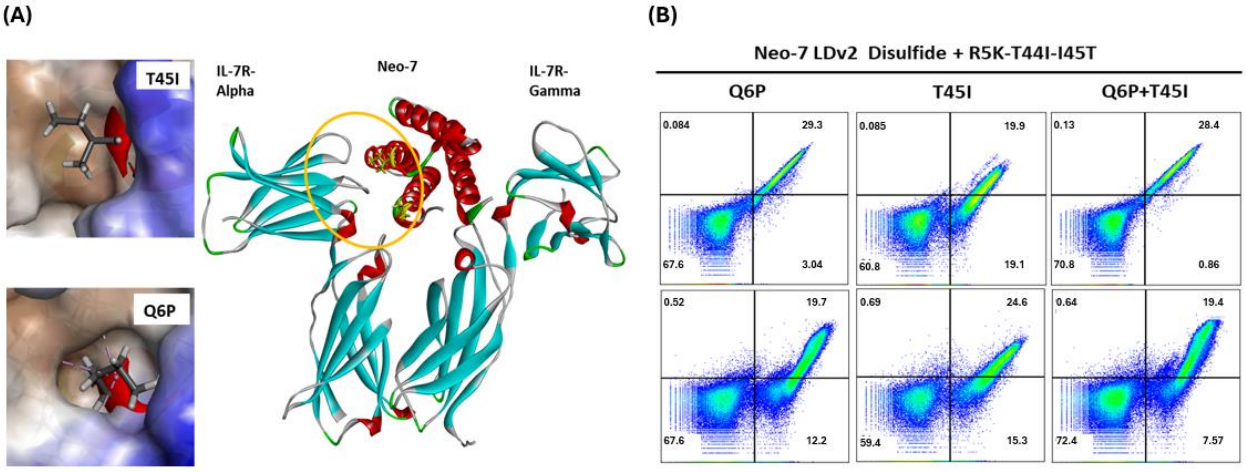

Figure 4. Validation of amino acid mutations that confers to the binding affinity of Neo-7 towards IL-7 receptor alpha and gamma. (A) Inspection of structural and binding interactions of residue mutations Q6P and T45I on Neo-7 towards the murine IL-7R alpha. (B) Yeast display and flow cytometry validation of the binding ability of IL-7/Neo-7 variants toward the IL-7 receptors.

Recombinant Neo-7 shows higher expression and thermostability than WT IL7

238 After validating Neo-7's ability to bind both IL-7Rα and IL-2Rγ receptors, we aimed to express
239 recombinant Neo-7 in *Escherichia coli*. Wild-type cytokines from the IL-2 family (IL-2, IL-7, IL-15, and
240 IL-21) are often challenging targets for *E. coli* expression due to their complex folding requirements,
241 which necessitate multiple disulfide bonds to stabilize their structures. For instance, WT-IL-7 contains
242 three disulfide bridges, and its soluble expression in *E. coli* yields no detectable properly folded IL-7, as
243 analyzed by FPLC after pre-purification using Ni-NTA affinity chromatography (**Figure 5A-B**). In
244 contrast, Neo-7 was engineered with only one disulfide bridge and designed for more efficient folding and
245 packing compared to WT-IL-7 (**Figure 5C-D**). Indeed, Neo-7 demonstrated superior performance in
246 terms of yield and purity. The Q6P variant of Neo-7 exhibited the highest purity (78.51%) and yield (1.56
247 mg/200 mL culture), while the double mutation variant (Q6P + T45I) showed lower purity (58.24%) and
248 yield (0.36 mg/200 mL). In comparison, WT-IL-7 was expressed as inclusion bodies, solubilized using
249 6M guanidine HCl, and refolded via dialysis, resulting in a final yield of 0.23 mg/200 mL culture with a
250 purity of 34.66% (Figure 5I). We also assessed the thermostability of the purified recombinant proteins
251 using the SYPRO assay. As expected, both Neo-7 variants exhibited improved thermostability (71.12°C
252 and 70.39°C for the single and double mutation variants, respectively) compared to WT-IL-7 (56.35°C;
253 Table 2). These results confirm that our novel designs confer better protein packing and higher stability
254 than WT-IL-7.
255
256 **Recombinant Neo-7 shows enhanced binding affinity to IL-7 receptor alpha than WT IL7**
257
258 We then characterized the binding affinities of Neo-7 variants to mouse IL-7 receptor alpha (mIL-7Rα) in
259 a quantitative manner. The dual mutant variant of Neo-7 exhibited the most potent binding to mIL-7Rα,
260 with a dissociation constant (KD) of 3.12 nM, followed by the Q6P variant (KD = 5.22 nM) and WT-IL-7
261 (KD = 13.4 nM; **Figure 5E-G**). Interestingly, through the SPR curve, we observed different binding
262 kinetics between WT-IL-7 and the Neo-7 variants. WT-IL-7 binds to IL-7Rα through a fast-on-fast-off
263 kinetic model. In contrast, Neo-7 variants displayed a slower on and off rate, with an approximately five

times lower on-rates (ka) compared to WT-IL-7 (1.03 x 10^6 and 1.38 x 10^6 $M^{-1}s^{-1}$ for Neo-7-Q6P and Neo-7-Q6PT45I, respectively, versus 5.86 x 10^6 $M^{-1}s^{-1}$ for WT-IL-7). However, Neo-7 variants also demonstrated significantly slower off-rates (kd) (6.313 x 10^{-3} and 4.296 x 10^{-3} s^{-1} for Neo-7-Q6P and Neo-7-Q6PT45I, respectively, compared to 7.844 x 10^{-2} s^{-1} for WT-IL-7). The details of the on and off-rates of the binding kinetics are shown in Supplementary Table 1. This slower dissociation rate compensates for the slower association rate, resulting in more potent overall binding affinities. To assess the biological functions of Neo-7 variants, we then used the IL-7-dependent cell line 2E8 for a cell-based proliferation assay (**Figure 5H**). The potency of the Neo-7 variants in stimulating 2E8 proliferation is correlated with their binding kinetics determined by the SPR assay. At high concentrations (10 ng/mL), the differences in proliferative abilities were insignificant, likely due to saturation of the cytokine. However, at lower concentrations (1 ng/mL), the differences became more pronounced, with Neo-7 variants demonstrating stronger pro-survival signals compared to WT-IL-7. Encouraged by the promising binding affinity data from SPR and 2E8 bioassay, we then submitted the sequence of WT-IL7 and Neo-7s into Immunomedicine group server for protein immunogenicity prediction. The predicted output showed that WT-IL7 is the most immunogenic with 6 potential antigenic fragments while the designed Neo-7s had 3 segments which all overlapping with the WT-IL7 antigenic fragments, indicating no additional immunogenic peptide fragments were introduced throughout the engineering processes of Neo-7 (Supplementary Figure S2A-D).

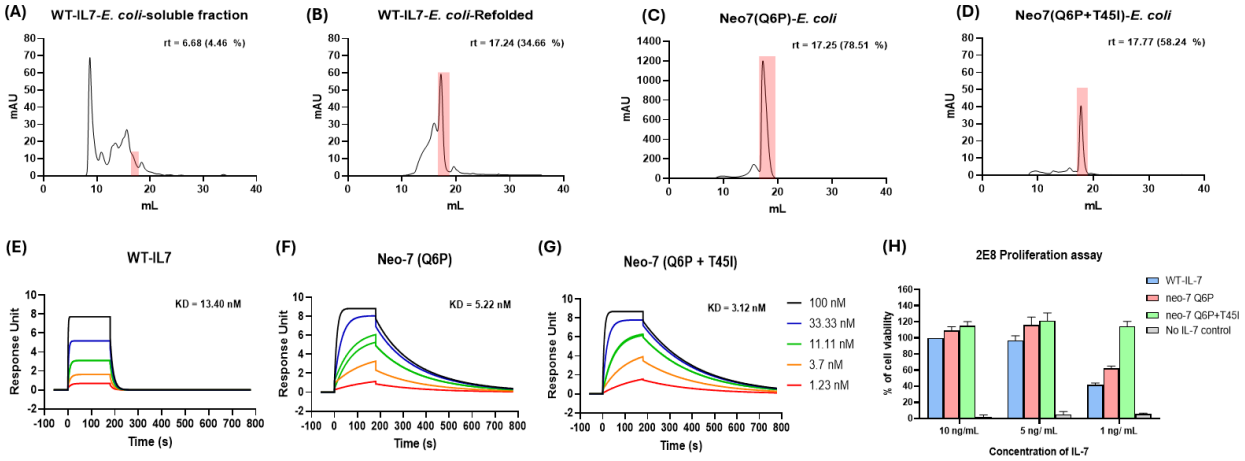

Figure 5. Characterization of *E. coli* expressed IL-7 and Neo-7s and the *in vitro* biological activities. FPLC profile of *E. coli* expressed (A) WT-IL7 (B) refolded WT-IL7 (C) Neo-7-Q6P and (D) Neo-7-Q6P-T45I. Percentage of purity is calculated from the SEC-FPLC peak profile via Cytiva Unicorn™ 7 software after affinity chromatography purification. SPR (Biacore) characterization of the binding kinetics of (E) Neo-7-Q6P (F) Neo-7-Q6P-T45I and (G) WT-IL7 towards murine IL-7R alpha. (H) 2E8 proliferation assay to investigate the biological activity of the IL-7/Neo-7s expressed by *E. coli*.

Table 2. Yield, purity and thermostability data of the *E. coli* expressed IL-7/Neo-7s, yield was presented as mg of recombinant protein per 200 mL of *E. coli* culture.

	Culture Volume	Expression mode	Yield after Ni-NTA purification	Yield after FPLC	Purity before FPLC (%)	Thermostability (Melting temperature)
Neo-7 (Q6P)	200 mL	Soluble	3.76	1.56	78.26	71.12
Neo-7 (Q6P+ T45I)	200 mL	Soluble	1.67	0.36	58.24	70.39
WT-IL7	200 mL	Refolding	7.41	0.23	23.24	56.35

Fc-fused Neo-7s shows superior yield and purity profile in CHO-expression system

Subsequently, we designed a Fc-fused neo-7/WT-IL7 for *in vivo* anti-tumor assay and express the recombinant protein in a CHO-cell based system. Immunomodulatory cytokines are attractive anti-tumor agents due to their immuno-stimulating potential, but the *in vivo* efficacies are largely limited by their poor pharmacokinetic properties that resulted in rapid clearance from the circulatory system. We therefore fused WT-IL7 and the selected neo-7 variants with the Fc-fragments of human IgG1 as a half-life prolonging strategy [26-28]. The fused Fc fragments were engineered with LALAPG mutations to attenuate Fc-mediated effector functions to prevent unintended cellular cytotoxicity in the host [29]. A structural illustration generated by alphafold simulation is shown in Supplementary Figure S2E. During recombinant protein expression, Fc-fused WT-IL7 exhibited a poorer purity profile (31.84%) compared to

305 the Neo-7 Q6P variant (80.88%) and the double mutation variant (55.15%), indicating that the superior
306 production yield and purity of Neo-7 extend beyond prokaryotic systems to mammalian CHO-S cell lines
307 (Figure 6A-C). Following FPLC purification, we assessed the bioactivities of the isotype control, Fc-
308 fused IL-7, and Neo-7 variants using a murine spleenocyte proliferation assay, with flow cytometry
309 evaluating viability and cell count at Day 3 and Day 7 post-treatment (Figure 6D-E). All treatments
310 maintained spleenocyte viability and numbers relative to the isotype control, with a slight but not
311 statistically significant increase in CD45+ cells in the Fc-Neo-7-Q6PT45I group. Our findings
312 demonstrate that Neo-7 variants offer superior yield and purity compared to WT-IL7 in both bacteria
313 (Table 2) and mammalian expression systems (Table 3).
314
315 **Fc-fused Neo-7s shows superior ability to promote T-cells expansions in B6 mice**
316
317 After validating the biological functions of the Fc-fused cytokines *in vitro*, we then investigated their *in*
318 *vivo* effects on the immune cell composition in mice peripheral blood. Each mouse received a single
319 intraperitoneal dose of 10 mg/kg Fc-fused IL-7 or Neo-7 variants. Blood samples were collected before
320 treatment (D0) and at 3, 7, and 12 days post-treatment to analyze immune cell composition. We focused
321 on CD45+ cells as an indicator of total immune cells and further examined the subpopulations and
322 numbers of CD3+ CD4+ T-cells, CD3+ CD8+ T-cells, and CD3- NK1.1+ NK cells, which are the
323 primary effector cell types contributing to the therapeutic effects of cytokine therapies. As shown in
324 Figure 6F-I, all treatments exhibited a similar pattern of increased CD45+ immune cells, peaking 7 days
325 post-treatment. Both Fc-fused Neo-7 variants induced significantly higher levels of CD45+ immune cells
326 compared to Fc-WT IL-7 treatment, particularly in the CD8+ T cell subpopulation.
327

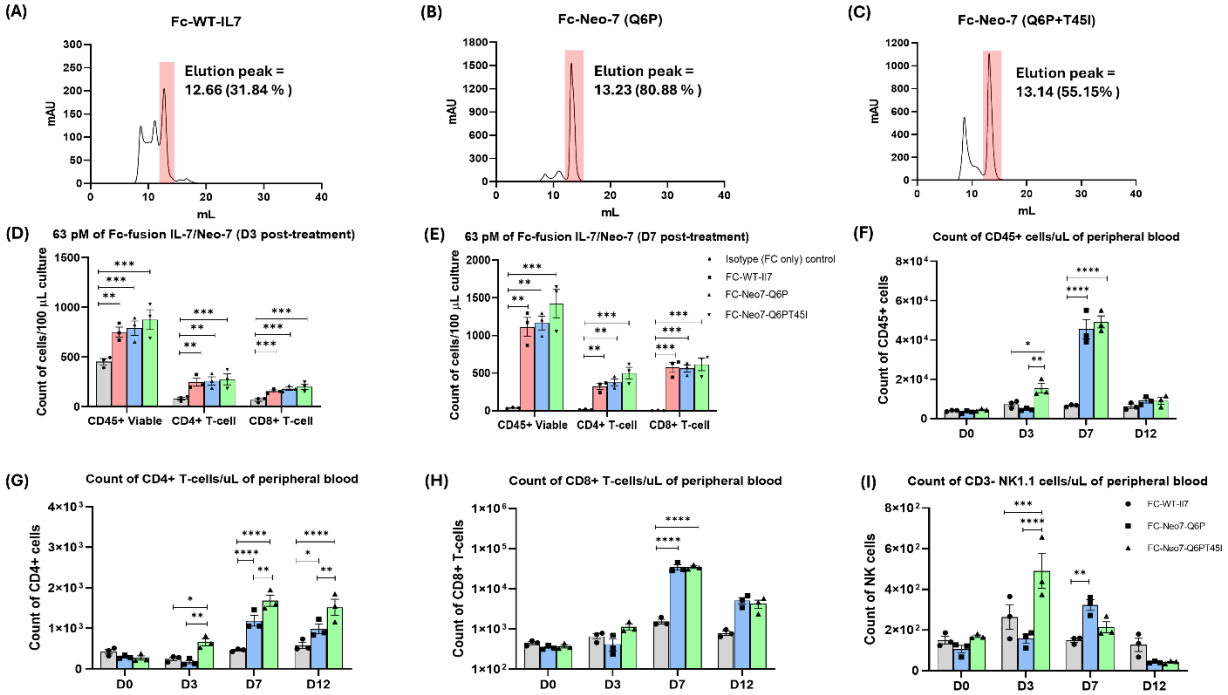

Figure 6. Characterization of CHO-S cells expressed FC-fused cytokines and their *in vitro* and *in vivo* biological activities. FPLC profile of CHO-S expressed (A) WT-IL7 (B) Neo-7-Q6P and (C) Neo-7-Q6P-T45I. Percentage of purity is calculated from the SEC-FPLC peak profile via Cytiva Unicorn^{TM} 7 software after affinity chromatography purification. Murine spleenocyte proliferation assay to investigate the biological activity of the Fc-fused IL-7/Neo-7s at (D) day 3 and (E) day 7 post-treatment. *In vivo* immune stimulatory ability of the Fc-fused cytokines on murine PBMCs at day 0 to day 12 post-treatment. The data are presented as count of (F) total viable CD45+ cells (G) viable CD45+ CD3+ CD4+ T-cells (H) viable CD45+ CD3+ CD8+ T-cells (I) viable CD45+ CD3- NK1.1+ NK-cells. All data were presented as individual data plots with error bars (SEM). Statistical differences among groups were determined using one-way ANOVA with Turkey's multiple comparison test. Significance levels are defined as follow *$p < 0.05$; **$p = 0.01–0.05$; ***$p = 0.0001–0.001$; and ****$p < 0.0001$.

Table 3. Yield and purity data of the CHO-S expressed Fc-fused IL-7/Neo-7s, yields were presented as mg of recombinant protein per 100 mL of CHO cell culture.

	Culture Volume	Expression Host	Yield after Protein A affinity purification/100 mL culture	Yield after FPLC purification/100 mL culture	Purity from FPLC Curve (%)
Neo-7-Fc	130 mL	CHO	15.73	10.44	80.88
Neo-7 T43I-Fc	130 mL	CHO	16.66	6.42	55.15
WT-IL7-Fc	130 mL	CHO	17.22	3.37	31.84

Fc-fused Neo-7s shows stronger anti-tumor activity in comparison to the WT counterpart.

Given the superior immune stimulatory effects of Fc-fused Neo-7s compared to Fc-WT-IL7, we hypothesized that these effects could translate into enhanced anti-tumor activity. To test this, we treated mice bearing subcutaneous MC38 tumors (a syngeneic model for colorectal cancer) with a single dose of 10 mg/kg Fc-fused IL-7 or Neo-7s and monitored tumor growth. All Fc-fused IL-7 treatments showed significant tumor suppression compared to the isotype control (human IgG-1 Fc with LALAPG mutation), with Fc-fused Neo-7 (Q6PT45I) being the most potent, followed by Fc-fused Neo-7 (Q6P) and Fc-fused WT-IL-7 (Figure 7A, Supplementary Figure S4).

To explore the possible anti-tumor mechanisms, we conducted a replicate anti-tumor assay and analyzed leukocyte counts and populations in the peripheral blood and tumor of treated mice. We found that the count and proportion of total immune cells and CD3+ CD8+ T-cells within the tumor correlated directly with the anti-tumor potency of the treatment groups (Figure 7C). In the peripheral blood of tumor-harboring mice, all Fc-cytokine fusions increased the total immune cell count compared to the isotype control, in the order of Fc-Neo7-Q6P-T45I, Fc-Neo7-Q6P, and Fc-WT-IL-7 (Supplementary Figure S3). This trend was also observed for CD4+ T-cells, CD8+ T-cells, CD19+ B-cells, CD11c+ dendritic cells, and F4/80+ macrophages. Among the immune cells analyzed, CD8+ T-cells showed the most significant increase, indicating they might be the primary targets for the immune stimulatory effects of IL-7/Neo-7s (Figure 7B). No significant differences were observed in the count of Ly6C+ Ly6g- CD11b+ monocytes in the peripheral blood (Supplementary Figure S3A). However, differences were observed between the

367 single (Q6P) and double (Q6P-T45I) mutation variants of Fc-fused Neo-7 in the numbers of CD4+
368 FoxP3+ Treg and CD3- NK1.1+ NK cells within the peripheral blood. The Q6P variant showed the
369 highest number of Tregs and NK cells among all treatment groups, followed by WT-IL7 and the Q6P-
370 T45I variant. Additionally, only mice treated with Fc-WT-IL7 had significantly higher numbers of Ly6g+
371 CD11b+ neutrophils compared to other treatments (Supplementary Figure S3A). These differences in
372 immune cell regulation might be attributed to variations in binding affinity or kinetics of WT-IL-7 and
373 Neo-7s towards IL-7 receptors on immune cells. Further studies are required to unravel the specific
374 mechanisms underlying this phenomenon.
375
376 In the analysis of tumor-infiltrating leukocytes, we found that only CD8+ T cells were significantly
377 enriched in the tumor compared to the isotype control (except for CD19+ B-cells in the Fc-Neo-7-Q6P
378 group), despite a substantial increase of other immune cell types (CD4+ T cells, macrophages, and NK
379 cells) in the peripheral blood (Figure 7B-C). This indicates that CD8+ T cells are the primary immune
380 effectors that infiltrate and contribute to the anti-tumor properties of the Fc-Neo-7 fusions. The CD8+
381 TILs were also differed in their effector status, where the perforin positive CD8+ populations were the
382 highest in the Fc-Neo-7-Q6PT45I group, followed by Fc-Neo-7-Q6P, Fc-WT-IL7 and isotype control.
383 Furthermore, only the Fc-Neo-7 fusions showed a significant reduction of the proportion of the
384 monocytes and neutrophils within the tumor compared to the isotype control, a phenomenon not observed
385 in mice treated with Fc-WT-IL7. The reduction of intra-tumoral monocytes and neutrophils-to-CD8 T cell
386 ratio is a favorable outcome for immunotherapy, as both of these immune cell types have been reported to
387 act as immunosuppressors, inhibiting the cytotoxic activity of CD8+ T cells within the tumor
388 microenvironment (Figure 7C) [30-32].
389
390

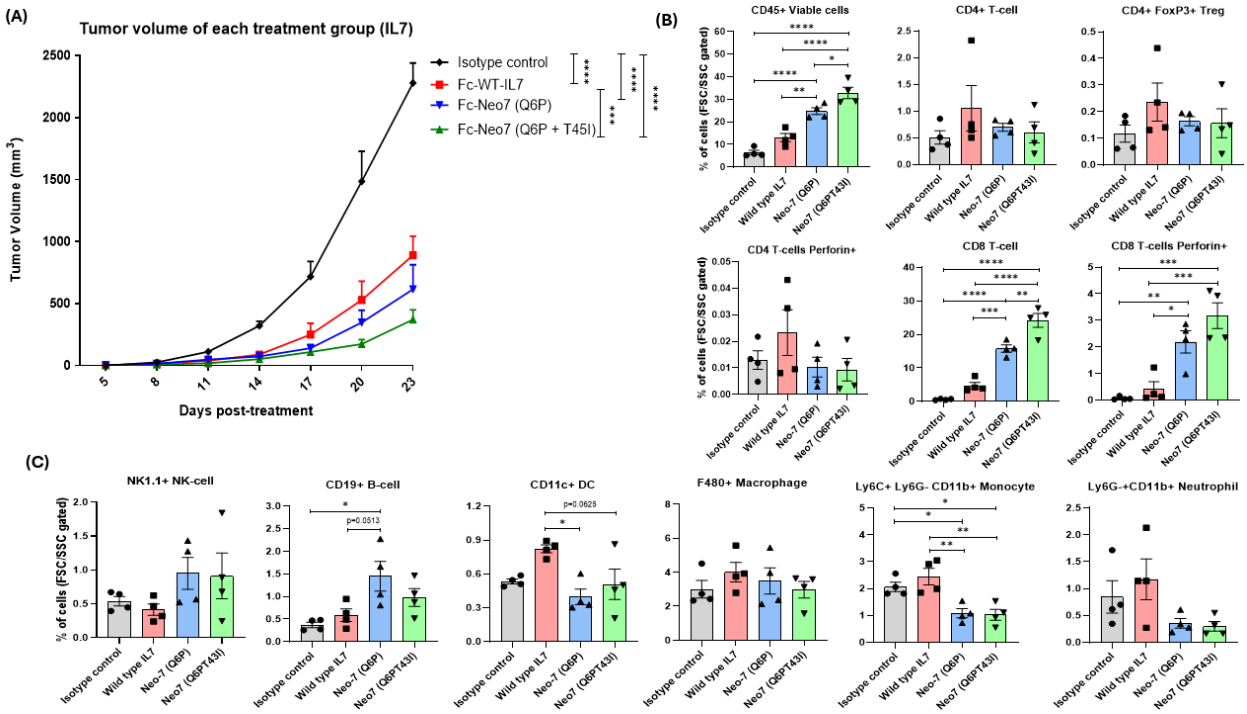

Figure 7. *In vivo* anti-tumor activity of Fc-fused WT-IL7/Neo-7s towards MC38 syngeneic models. (A) Tumor growth curve of MC38 tumor after treatment with the Fc-fused cytokines. Proportion of total leukocytes and different immune cell types within the MC38 tumor of mice at day 7 post-treatment. (B) Proportion of intratumoral CD4+ and CD8+ T-cells (C) Proportion of other immune cell types present in the TME at day-7 post treatment. All data were presented as individual data plots with error bars (SEM). Statistical differences among groups were determined using two-way ANOVA and one-way ANOVA with Turkey's multiple comparison test for tumor growth curve and TILs analysis respectively. Significance levels are defined as follow *$p < 0.05$; **$p = 0.01–0.05$; ***$p = 0.0001–0.001$; and ****$p < 0.0001$.

Since IL-7 is also known to promote the generation and maintenance of memory T cells, we also investigated the naive and memory populations of T cells using CD44 and CD62L markers (Supplementary Figure S3B-C). Most of the CD4+ T cells circulating in the peripheral blood of the isotype control group were naive T cells (CD62L+ CD44-). However, treatment with Fc-IL-7/Neo-7s increased the number of effector memory (EM) populations (CD62L- CD44+). For CD8+ T cells, treatment with the Fc-cytokine fusion greatly enriched the CD8+ T cell population with a central memory (CM) phenotype (CD62L+ CD44+), followed by naive and effector memory T cells. In the MC38 tumor, most infiltrating T cells were identified as effector memory T cells. The majority of CD4+ tumor-

409 infiltrating T cells exhibited an EM phenotype, with one exception showing a higher number of naive
410 CD4+ T cells in mice treated with Fc-WT-IL7. For tumor-infiltrating CD8+ T cells, nearly all were
411 positive for the memory marker CD44, with the main populations being EM CD8+ T cells (CD62L-
412 CD44+), followed by CM CD8+ T cells (CD62L+ CD44+).
413
414 **Fc-Neo-7 (Q6P-T451) greatly enhances expression of genes related to T-cells proliferations and**
415 **effector functions without up-regulation of exhaustion-related genes.**
416
417 To further investigate the differences between the treatment effects of Fc-Neo7 (Q6PT43I), Fc-IL-7, and
418 the isotype control, we conducted an RNA-sequencing experiment on the splenic CD8+ T cells of the
419 treated mice. CD8+ T cells were chosen due to their significant responsiveness to the treatments and their
420 abundance in the spleen, ensuring sufficient RNA for sequencing. Principal component analysis (PCA) of
421 the RNA-seq data revealed distinct RNA expression profiles for each treatment group, with clear
422 clustering and segregation among the groups (Figure 8A). Gene ontology (GO) analysis of the
423 differentially expressed genes showed that both Fc-IL-7 and Fc-Neo-7 upregulated genes related to
424 immune system processes, immune responses, and inflammatory responses relative to the isotype control.
425 Comparing Fc-IL-7 and Fc-Neo-7, we found that genes related to cell proliferation (cell cycle, cell
426 division, and DNA replication) were the most prominently upregulated, corroborating our *in vivo* PBMC
427 proliferation assay data (Figure 8B).
428
429 Further examination of the gene expression heatmap (Figure 8C) showed strong differentiation in the
430 gene expression profile among the two Fc-Neo-7 variants with Fc-WT-IL7. Gene clusters associated with
431 T cell proliferation, fitness, and functionality revealed that Fc-Neo-7 treatment upregulated cell cycle-
432 related genes (Cdk2, Cdk4, Cdk6, Mki67) and pro-survival signals (Bcl-2, Brca1, survivin/BirC5) [20,
433 33-35]. In addition, a general increase in the expression of genes related to T-cell metabolisms were also
434 observed, including those regulating oxidative phosphorylation, fatty acid oxidation, amino acid (glycine,

435 serine threonine pathway) and nucleotide metabolisms, indicating an active proliferation and metabolism
436 stage of the CD8 T-cells post-FC-Neo-7 treatments [36-38]. The serine to glycine one-carbon metabolism
437 pathway was essential to support T cell proliferation by fueling purine biosynthesis and improving
438 mitochondrial respiration efficiency [39, 40]. Fc-Neo-7 also primed T cells for enhanced functionality, as
439 evidenced by the upregulation of genes responsible for cytotoxicity (granzymes A, B, and C) and surface
440 receptors for IL-2 (IL2Ra, IL2Rb) and IL-12 (IL12rb), which prepared T cell differentiation into effector
441 types. Notably, while IL-2-induced T cell proliferation often leads to exhaustion and activation-induced
442 cell death (ACID), Fc-Neo-7 treatment resulted in reduced expression of inhibitory molecules (Tgfbr2,
443 Lag3, CD83, PD-1) except TIGIT [41, 42]. This suggests a potential combination therapy of Fc-Neo-7
444 with anti-TIGIT to further enhance CD8+ T cell effector activity by blocking the immunosuppressive
445 TIGIT pathway. In terms of exhaustion markers, Fc-Neo-7-treated CD8+ T cells exhibited marked
446 reductions in the expression of genes such as Tim-3 (Havcr2), Tox, and CTLA4 [41, 42]. These findings
447 were also confirmed by GSEA analysis, which showed significant enrichment of gene sets related to cell
448 cycle and DNA replication (T cell proliferation), oxidative phosphorylation, and fatty acid metabolism
449 (naïve T cell metabolism). In addition, a lower expression of the genes related to the PD1-PDL1
450 inhibitory axis was also observed (Figure 8D).
451

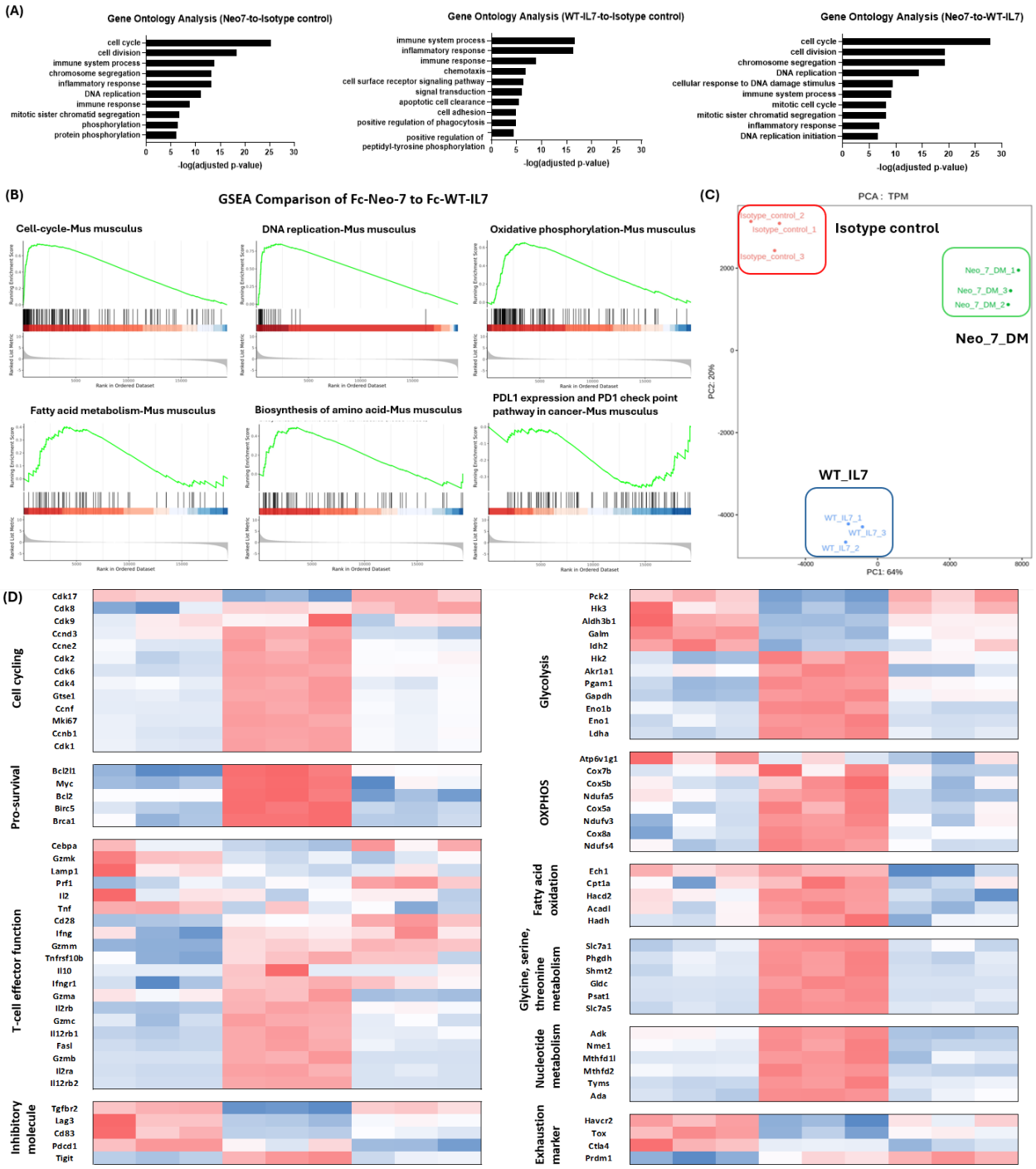

Figure 8. RNA-sequencing of splenic CD8+ T-cells isolated from Fc-IL7/Neo-7s treated mice. (A) gene ontology analysis of the gene expression data from RNA sequencing (n = 3; three independent biological donor for each group). (B) Gene Set Enrichment Analysis (GSEA) of splenic CD8+ T-cells treated by Fc-Neo-7 versus Fc-WT-IL7. (C) principal component analysis and (D) Gene expression heatmap derived from Z-scores calculated from the RNA sequencing data.

460 **Discussion**

461

462 Cytokines are potent immunomodulatory proteins that serve as attractive therapeutic agents in numerous
463 disease applications. However, clinically their application is limited due to the need to balance the clinical
464 potency to toxicity and poor pharmacokinetics [7, 18, 43]. In this study we ~~attempted to~~ addressed these
465 issues through (1) proper selection of a relatively safe cytokine, IL-7 and (2) redesign the scaffold of IL-7
466 via computational protein design to improve the stability and developability of the final molecule, Neo-7.
467 Throughout the design process, we observed that the original structure of scaffold of WT IL-7 is complex
468 and very inefficient, involving long inter-helices loops that required additional disulfide stapling to ensure
469 proper folding. Since only the helices of IL-7 are required for receptor binding, we chose to truncate all
470 the interconnecting loops and remodel the helices connectivity via Rosetta loop remodeling program. The
471 difference between the design of IL2/15 mimics (Neo 2/15) and this study lies on the design approaches,
472 Neo2/15 was a completely *de novo* designed protein which requires to redesign the mimetics from scratch
473 while the Neo-7 designed in this study still retains the sequence on the functional-related moiety (receptor
474 binding helices) and thus minimizing the design steps and computational power required [11]. However, it
475 should be noted that our study has a somewhat different objective in that the Neo2/15 is a product from
476 the breakthrough invention of the *de novo* protein design algorithm from the Baker lab while the aim of
477 this study is to search for a viable design idea that utilize the availability of CPD toolkits such as
478 alphafold and Rosetta protein design suite for the redesign of a therapeutic-relevant cytokine.

479

480 In our approach, we avoided the need for extensive rounds of directed evolution and affinity maturation
481 process. During the design process, we utilize Alphafold2 to serve as a validation point for our designed
482 sequence. We observed that single sequence mode of Alphafold2 provided a better discriminative power
483 on the designed sequence as the default mode of Alphafold2 (with reference to the MSA library) provide
484 higher false positive results (bad sequence generating very similar structure to the WT-IL7 helices),
485 possibly due to the highly similar sequences between the WT-IL7 and Neo-7. In addition, we also

486 discovered the presence of a kink on helix 1 is crucial for the interaction between the IL-7Rα and IL-
487 7/Neo-7, the re-addition of the kink in helix1 via disulfide stapling and mutation transfer guided by
488 structural visual inspection generated two Neo-7 variants that are more potent in IL-7R binding affinity in
489 comparison to the WT-IL7. Encouragingly, both the Neo-7 variants are also more thermostable compared
490 to the WT-IL-7 and showed a much higher yield and purity when expressed in *E. coli* (as single entity)
491 and in CHO cells (as Fc-Fusion) indicating that the simpler protein scaffold of Neo-7s are much better
492 handled by the cellular machineries during overexpression. Interestingly, the redesigned scaffold of Neo-
493 7s lead to a different binding kinetics towards, IL-7Rα in comparison to the WT-IL7. The Neo-7s adopted
494 a slow-on-slow-off model, which we ascribed to the more stable fold as a more flexible (less stable) fold
495 in the WT-IL7 could probably increase the chances to bind to the IL7Rα via an induced-fit mechanism
496 but the overall flexibilities of the protein will also lead to stronger destabilization of the protein-receptor
497 complex and therefore lead to a faster off-rate [25, 44]. In contrast, a more stable fold adopted by the
498 Neo-7s would require longer time for the protein-receptor association but also a slower dissociation rate
499 once the complex have been formed [45, 46].
500
501 Moreover, the comparison of the *in vitro* and *in vivo* efficacies of the Fc-Neo-7s and Fc-IL-7 also
502 highlighted the importance of *in vivo* stabilities during animal studies. *In vitro* murine spleenocytes
503 proliferation assays showed no significant differences between the samples treated with Fc-Neo-7s and
504 Fc-IL-7 but the *in vivo* PBMC analysis showed a significant increase in the count of CD8+ T-cells
505 (peaked at day 7), possibly due to the better stability of Fc-Neo-7s in the mice circulatory system.
506 Encouragingly, the *in vivo* immune stimulation activities of the Fc-IL-7/Neo-7s also translated into anti-
507 tumor activities where the efficacy of tumor growth delay was correlated with the binding affinities to IL-
508 7Rα determined in the yeast display and SPR assays. Further analysis of the TILs also revealed a
509 significantly higher infiltrations of the CD8+ T-cells in the tumor and the higher proportion of Perforin +
510 CD8+ T-cells also suggest that the T-cells induced by Fc-Neo-7s treatment are functional in terms of

511 cancer cells cytotoxicity. Moreover, gene expression profile of the murine CD3+ CD8+ spleenocytes also
512 revealed that Fc-Neo-7 (Q6PT45I) significantly upregulates genes related to CD8+ T-cells proliferation
513 and metabolism without affecting their fitness and functionality, suggesting that Neo-7 (Q6PT45I) as a
514 suitable addition to the current therapeutic space for cancer treatment. To further assess the role of Fc-
515 Neo-7 (Q6PT45I) as an additional arm in anti-cancer therapy, we combined one dose of the Fc-Neo-7
516 (Q6PT45I) with oxaliplatin, a first-line immunogenic chemotherapy for colon cancer. Indeed, the
517 combination therapy showed a significantly stronger tumor suppressing result in comparison to the
518 untreated control and the monotherapy arms (Supplementary Figure S5).
519
520 In conclusion, we have successfully redesigned IL-7 with a novel folding scaffold termed Neo-7 in this
521 study. Through Rosetta fix backbone modeling and visual inspection, we further identified that the
522 disulfide-induced kink on helix 1 is essential for the binding towards IL-7Rα and point mutations R5K,
523 Q6P and T44I could enhance the binding of Neo-7 towards IL-7Rα. The point mutation I54T, improved
524 the stability, yield and purity of Neo-7 but with a slight penalty on the binding strength with the IL7Rα.
525 The designed Neo-7s were also proven to be more potent, stable and easier to be expressed in both the *E.*
526 *coli* and CHO systems, highlighting the importance of inherent protein stability in recombinant protein
527 expression. Since the four helical bundle is a common type of protein fold in the interleukin family (i.e.
528 IL-6, IL-9, IL-21, GMCSF and etc.) the concept of the current designs could be further applied into the
529 designs of other types of neo-interleukins to deepen the involvement of computational protein design in
530 the protein therapeutics area and broaden the horizon of interleukin-based therapies in the future.
531
532
533 **Material and Methods**
534 **Helix definition and loop remodeling**

535 The PDB structure of human IL-7 with IL-7 receptor alpha (PDB ID: 3DI2) were downloaded and
536 inspected using Pymol visualizer. The helixes were defined as follows: helix 1 (residue 8 - 27), helix 2
537 (residue 51 - 66), helix 3 (residue 73 - 91) and helix 4 (127 -149) adopting the residue numbering of the
538 PDB file (3DI2) [25]. The connecting loops were removed, and each helix was rejoined in a clockwise
539 manner with the orientation of H1 > H3 > H2 >H4. The new loops were remodeled using Rosetta
540 Remodel program
541 (https://www.rosettacommons.org/docs/latest/application_documentation/design/rosettaremodel#code-
542 and-demos) according to the developer instructions [47]. The design of the remodeled protein was
543 furthered optimized via visual inspection and Rosetta fix backbone design according to the developer
544 instructions (https://www.rosettacommons.org/docs/latest/application_documentation/design/fixbb). The
545 amino acid sequence of each protein structure output in the intermediate steps of design were extracted
546 and fed to Alphafold2 program for protein structure prediction [48, 49]. The outputs were then aligned to
547 the structural template generated from Rosetta fix backbone design using pymol visualizer and the protein
548 design is accepted when the protein structures generated from both programs aligned well with each other
549 with a RMSD value <1.0 [50]. In this study, despite the human IL-7 was used as a template for Neo-7
550 design, mouse IL-7 receptors were used for *in vitro* validations as human IL-7 cross reacts with mouse IL-
551 7 receptors and such designs ensure the consistency between the *in vitro* and the *in vivo* studies.

552

553 **Prediction of protein structure using Alphafold2 and Alphafold Multimer**

554 Alphafold 2 was used for the validation of our protein designs. For monomer prediction, Alphafold were
555 ran using google collab with the following settings. First, a non-template and single sequence mode was
556 applied to predict the structure of Neo-7. We hypothesized that since the sequence of Neo-7 is highly
557 similar to the wild type IL-7, the information from PDB structural template and multiple sequence
558 alignment (MSA) might highly favors the generation of the predicted structures that are highly similar to
559 the wild type structure and thus lead to a reduced ability to discriminate the bad structures from the good.

560 (https://colab.research.google.com/github/sokrypton/ColabFold/blob/main/AlphaFold2.ipynb#scrollTo=G
561 4yBrceuFbf3) [51]. On the other hand, predictions using Alphafold multimer was done in local
562 workstation with template mode querying through a full database for maximal accuracy of the prediction.
563 (https://github.com/google-deepmind/alphafold) [48, 49].

564

565 **Molecular cloning of neo-7 variants**

566 The amino acid sequences of the selected neo-7 designs were reverse translated into nucleotide sequences
567 using IDT codon optimization tools (https://sg.idtdna.com/CodonOpt) and the transgenes were
568 synthesized in the form of gBlock followed by cloning into a Aga2-SP based yeast display vector through
569 Gibson assembly. The resulting plasmids were then transformed into *E. coli* (XL10-gold strain) and plated
570 on ampicillin plate (100 µg/mL) for overnight selection. Two colonies were picked and cultured overnight
571 in LB medium supplemented with 100 µg/mL ampicillin for DNA isolation and sequencing.

572 **Yeast transformation and induction of yeast-displayed proteins**

573 Yeast (strain EBY100) is cultured and maintained in YPD medium consisting of 2% dextrose, 2% peptone
574 and 1% yeast extract at 30 ^{o}C with 150 rpm of shaking. A lithium acetate (LiAc) method was applied for
575 yeast transformation. Briefly, yeast was cultured in YPD overnight followed by 1:50 dilution in fresh
576 YPD medium the next day. The diluted culture was grown to early log phase (OD600 = 0.2) prior to the
577 transformation. One mL of culture is required for one transformation. The culture was spun at 3000 xg for
578 2 min followed by two rounds of washing, using 1 mL of sterile water and 0.5 mL of LiAc/TE solution
579 (10 mM Tris-HCL, 100 mM LiAc, and 1mM EDTA). The washed yeast was then pelleted and
580 resuspended with 60 µL of LiAc/TE solution, 25 µL of ssDNA and 200 ng of the desired plasmid. The
581 mixture was mixed via pipetting followed by addition of 220 µL of PEG solution (40 % w/v PEG3350
582 dissolved in LiAc/TE solution). The resulting samples were incubated at 30 ^{o}C for 30 min without
583 shaking followed by addition of 35 µL of DMSO and 15 min heat shock at 42 ^{o}C. The yeast suspensions

584 were then pelleted at 3000 xg for 1 min , resuspended with 200 μL of sdH_2O and plated on SDCAA plate
585 for drop out selection. For validation of the display of desired proteins on the transformed yeast, three
586 colonies were selected from the drop-out plate and cultured in SDCAA medium for two passage followed
587 by an 18 h induction in SGCAA medium (containing 2% galactose as inducing agent).

588 **Assessing expression level and receptor binding analysis of yeast-displayed neo-7 using flow**
589 **cytometry.**

590 Approximately 1 x 10^7 of the induced yeast culture (OD600 = 1 in 1 mL culture) were pelleted, washed
591 twice with 1X PBS and resuspended in 100 μL of 1X PBS in a 96-well v-bottom plate. Receptor binding
592 was done by incubation of yeast with a final concentration of 50 nM IL-7 receptor-α (IL7Rα; Sino
593 Biological Cat: 50090-M08H) consisting of a C-terminal polyhistidine tag for 30 min at 4 ^{o}C on a mini
594 shaker agitated at 600 rpm. The cells were washed and stained with Alexa Fluor 488 anti-HA.11 antibody
595 (Biolegend Cat: 901509; 1:100 dilution) and Alexa Fluor 647 anti-His Tag antibody (Biolegend Cat:
596 362611; 1:1000 dilution) for an additional 15 min at 4 ^{o}C to determine the expression level of the
597 displayed protein and their binding affinity towards IL-7 receptor-α. To assess the binding of the common
598 IL-2 receptor γ (IL2Rγ) to neo-7 and IL7Rα complexes, the yeasts were first incubated with 50 nM of
599 IL7Rα, washed and incubated with 100 nM of human-Fc tagged IL-2 receptor-γ (IL2Rγ; Sino Biological
600 Cat: 50087-M03H) at 4 ^{o}C for an hour. The yeast was then washed twice with 1X PBS and stained with
601 Alexa Fluor 647 anti-HA.11 antibody (Biolegend Cat: 682404; 1:200 dilution) and PE anti-human IgG-Fc
602 antibody (Abcam cat: ab131612; 1:10 dilution) for an additional 15 min to determine the expression level
603 of the displayed protein and their binding affinity towards IL-2 receptor-γ. The yeasts were then spun
604 down, washed twice with 1X PBS and assessed by flow cytometry. Flow cytometry data were analyzed
605 using FlowJo software. Yeast cells were first gated based on forward and side scatter to exclude debris
606 (FSC-A vs. SSC-A), followed by singlet gating (FSC-A vs. FSC-H). Surface expression and binding were
607 assessed using aforementioned fluorescent markers, and double-positive populations were quantified. The

608 full gating strategy is shown in Supplementary Figure S6.**Expression and purification of recombinant**
609 **Neo-7 in *E. coli* (BL21).**

610 The desired neo-7 gene designs were PCR amplified to generate amplicons with at least 20 bp
611 overlapping with the linearized bacteria expression vector. The incorporated transgenes were flanked by a
612 ST-II signal tag and a hexa-histidine tag at their 5' and 3' end to target the recombinant protein into the
613 periplasmic region for proper disulfide formation and to aid purification respectively. The recombinant
614 plasmid was transformed into *E. coli* BL21 competent cells and grew in LB-kanamycin (50 ug/mL)
615 medium for selection of transformant. On the day of protein expression, overnight culture of the bacteria
616 were diluted (1:200) in fresh 2X-YT medium supplemented with 25 ug/mL kanamycin and grown into log
617 phase (OD600 = 0.4-0.6) at 37 ^{o}C. The cultures were then transferred into a chilled incubator (18 ^{o}C) and
618 incubated for an additional 48 h for protein expression (no IPTG is required for expression). After
619 incubation, the cultures were pelleted at 8000 xg for 20 min, supernatant was discarded, and the pellets
620 were stored in -80 ^{o}C for overnight. The recombinant protein was purified using nickel NTA affinity
621 chromatography. The frozen pellets were thawed on ice for an hour followed by cell lysis using B-PER^{TM}
622 Bacterial Protein Extraction Reagent according to manufacturer protocol. The supernatant was collected
623 and incubate with the Ni-NTA resins (125 uL of resin for 100 mL of bacteria culture) at 4 ^{o}C for an hour.
624 The Ni-NTA column was washed with wash buffer until no A280 signal was observed from the eluate,
625 The recombinant proteins were then eluted with 5 mL of elution buffer. The eluate was then spun in
626 Amicon Ultra-15 centrifugal filter (3 kDa) to exchange the elution buffer with 1X PBS (pH 7.4) and to
627 concentrate the protein into a suitable volume size (600 uL) for FPLC purification using Superdex® 200
628 Increase 10/300 GL size exclusion chromatography column. On the other hand, similar procedure was
629 used for expression of WT-IL7, except that WT-IL7 was expressed as inclusion body and the inclusion
630 body was solubilized using 6M guanidine-HCL, purified using NI-NTA affinity chromatograpphy and
631 refolded in refolding buffer (100 mM Tris-HCL, 1mM EDTA, 250 mM L-arginine, 1 mM reduced
632 glutathione, 0.5 mM oxidized glutathione, 10 % v/v glycerol, pH 8.0) overnight at 4 ^{o}C. The refolded

633 protein was dialyzed 1 round against 100 mM Tris-HCL (pH 10) and another 3 rounds against 1X PBS
634 (pH 7.4) to remove the remaining additives. The refolded protein was concentrated and purified using
635 FPLC foe subsequent *in vitro* assays.

636 ***In vitro* validation of neo-7 bioactivity**

637 **2E8 proliferation assay**

638 2E8 cells (ATCC TIB-239), an IL-7 dependent murine B-cell cell line were cultured in Iscove's modified
639 Dulbecco's medium (IMDM; Gibco Cat: 12440053) supplemented with 0.05 mM 2-mercaptoethanol 2
640 ng/mL mouse IL7 (Sino Biological) and 20 % FBS. Proliferation assay was conducted using CCK-8 assay
641 kit. Briefly, 1 x 10^5 2E8 cells were incubated in 100 uL of medium containing 1 ng/mL and 10 ng/mL IL-7
642 in a flat bottom 96-well plate for 3 days in a humidified CO_2 incubator at 37 ^oC. 10 uL of the CCK-8
643 reagent was added into each well followed by an additional 3 hour incubation at 37 ^oC. The resulting
644 A450 signal was then read using Tecan infinite microplate readers and all data were analyzed using
645 GraphPad Prism 8.0.

646 **Murine Spleenocytes proliferation assay**

647 Spleens from C57BL/6J mice were harvested and grinded against a 40 um strainer for
648 spleenocyte isolation. The isolates were pelleted followed by lysis of red blood cells (RBC) and
649 cell counting. The spleenocytes were cultured in RPMI medium supplemented with 10% heat-
650 inactivated FBS, 0.05 mM β-mercaptoethanol, 10 mM HEPES, 2 mM glutamine, 0.1 mM
651 nonessential amino acids, 1 mM sodium pyruvate, and 1X insulin-transferrin-selenium (ITS). For
652 proliferation assay, 2 x 10^6 spleenocytes were incubated in 12 well plate with 1 mL of the culture
653 medium. All spleenocytes were treated with 1 ug/mL of anti-CD3 and anti-CD28 antibodies on
654 the first day for T-cell stimulation, supplemented with either 2 ng/mL or 20 ng/mL of WT-IL7 or

655 neo-7 variants. The resulting spleenocytes were counted using an automated cell counter and
656 split at a 1:5 ratio every three days into fresh medium containing freshly prepared IL-7.

657 **Surface Plasmon Resonance (SPR) analysis of neo-7 binding affinity to murine IL7Rα.**

658 SPR was conducted to determine the binding affinity of recombinant neo-7 variants to murine IL7Rα.
659 Neo-7 recombinant proteins were produced via *E. coli* as mentioned in the previous section. Recombinant
660 murine IL7Rα was diluted to 20 ug/mL in 10 mM sodium acetate (pH 4.5) and immobilized to a CM5
661 CHIP (Cytivia) via amine coupling. The maximum response unit (Rmax) was controlled to be below 30 to
662 reduce mass transport limitations according to the manufacturer protocol. A threefold serial dilution of
663 WT-IL7 and two neo-7 variants were performed in HBS-EP+ buffer and flowed passed (50 uL/min) the
664 immobilized chip with an association and dissociation time of 180s and 600s respectively. The chip was
665 regenerated by 30s exposure to 3M $MgCl_2$ with a flow rate of 10 uL/min. The binding affinity (KD) and
666 dissociation constants (Kd) were calculated using Biacore T200 evaluation software and the resulting
667 binding curves were regenerated using GraphPad Prism 8.0.

668 ***In vivo* validation of neo-7 bioactivity**

669 **Design and expression of recombinant Neo-7-Fc fusion**

670 Following the validation of the bioactivity of Neo-7, we proceeded to construct a Neo-7-Fc fusion protein
671 by fusing Neo-7 variants to the C-terminus of a human Fc fragment (with LALAPG mutation) using a 20-
672 amino acid glycine-serine linker $(GGGGS)_4$. The gene construct was then cloned into the pCDNA 3.4
673 vector and transfected into Chinese hamster ovary (CHO) cells for recombinant protein expression. The
674 Expifectamine™ CHO transfection kit was employed for transfection, following the manufacturer's
675 protocol. In brief, 100 µg of plasmid DNA was transfected into 100 mL of CHO cells pre-grown to a
676 density of 6 x 10^6 cells/mL. CHO-enhancer and feed were added at 16 hours post-transfection. The
677 culture was allowed to grow for an additional 10 days at 8% CO_2 with 150 rpm shaking. Subsequently,
678 the recombinant protein was purified using protein-G affinity chromatography, concentrated with an

679 Amicon tube protein concentrator, and further purified to achieve at least 95% purity using FPLC
680 chromatography. The resulting protein was eluted with 1X PBS (final concentration = 1 mg/mL), flash-
681 frozen using liquid nitrogen, and stored at -80°C for future use.

682 ***In vivo* validations of Neo-7 biological functions.**

683 All mice used in this study were wild type C57BL/6 (B6) strain and were procured from the National
684 Laboratory Animal Center (NLAC), NAR Labs, Taiwan. The mice were housed at the animal facilities of
685 the Institute of Biomedical Sciences, *Academia Sinica*, with maintained environmental conditions,
686 including proper temperature (19-23°C) and humidity (50-60%), under a 12-hour light-dark cycle. All
687 animal experiments were conducted at the animal house of the Institute of Biomedical Sciences,
688 *Academia Sinica*, in compliance with scientific and ethical guidelines, as approved by the institution's
689 Animal Care and Usage Committee.

690 **Peripheral blood immune cells analysis in murine model**

691 B6 mice received intraperitoneal injections of different variants of Neo-7-Fc fusions to assess the in vivo
692 biological effects of the designed proteins on the immune composition in mice peripheral blood. Each
693 mouse was administered 10 mg/kg of the respective treatments (Fc-only; Fc-WT-IL7; Fc-Neo-7-Q6P; Fc-
694 Neo-7-Q6PT45I). Peripheral blood samples were collected via submandibular blood collection before
695 treatment, as well as 3 days, 7 days, and 12 days post-treatment. The collected blood was preserved in an
696 EDTA tube (BD microcontainer) and subjected to immediate red blood cell (RBC) lysis, followed by flow
697 cytometry analysis to assess leukocyte populations.

698 ***In vivo* anti-tumor activity of Neo-7-Fc fusion protein in MC38 syngeneic models**

699 To induce tumor in mice, 1 X 105 of MC38/CT26 cells were lifted with versene, suspended in 1X PBS
700 and subcutaneously injected into the right flank of each mouse. Treatment was initiated at day-5 post-
701 tumor inoculation for tumor growth analysis and day-10 for combination treatment and TILs analysis.

702 Tumor volume (mm3) was calculated using the following equation: [(tumor length + tumor weight)/2]3 x
703 0.52. Mice with a tumor that was larger than 1500 mm3 were considered dead for ethical reasons.

704 **Tumor-infiltrating Leukocytes (TILs) Analysis**

705 The tumors from mice in different treatment groups were excised, weighted, and processed to obtain
706 tumor cell suspensions. The tumors were cut into small pieces, immersed in TILs buffer (composed of
707 670 μg/mL collagenase IV and 2 μg/mL DNase I dissolved in MC38 culture medium) and processed into
708 single-cell homogenates using the gentleMACSTM Octo Dissociator (Miltenyi Biotec Inc). The resulting
709 cell suspensions were passed through a 40 μm cell strainer, treated with 1X RBC lysis buffer, and
710 resuspended in FACS buffer (5% FBS in PBS, v/v, pH 7.2). All samples were blocked with CD16/32 Fc
711 blocker (1: 50 dilution) prior to immunostaining. For surface staining, the TILs were stained with
712 eFluor™780 eBioscience™-Fixable Viability Dye, Pacific Blue™-CD45 antibody, PerCP/Cyanine5.5-
713 CD45 antibody, APC-CD4 antibody, AlexaFluor®-CD8a antibody, Alexa Fluor®647-Ly6G antibody,
714 FITC-CD11B antibody, Pacific Blue-CD11B antibody, BrilliantViolet421-F4/80 antibody and FITC-
715 MHCII antibody. For intracellular staining, all samples were fixed and permeabilized with 4%
716 paraformaldehyde (PFA) and 0.1 % saponin respectively, after staining of the surface markers. The
717 samples were then stained with PE-IFN-γ antibody and Brilliant Violet 785™-TNF-α antibody. The
718 stained samples were analyzed using Attune NTX flow cytometer, and the data were processed using
719 FlowJo V10 software. The full gating strategy is shown in Supplementary Figure S7 and the absolute
720 count of the tumor-infiltrated immune cells are provided in Supplementary Figure S8.

721 **RNA sequencing of splenic CD8+ T-cells**

722 B6 mice were intraperitoneally treated with 10 mg/kg of the Fc-fused cytokines (Fc-only isotype control;
723 Fc-WT-IL-7 and Fc-Neo7-Q6PT45I). At day 7 post-treatment, mice were sacrificed and splenic CD8+ T
724 cells were isolated using EasySep^{TM} Mouse CD8+ T-cell isolation kit according to the manufacturer

725 protocol. The isolated CD8+ T-cells were then lysed using TRIzol™ reagent and sent to Genomics Inc
726 (Taiwan) for RNA isolation and RNA sequencing.

727

728 **Acknowledgements**

729 The work was supported by the National Science and Technology Council of the Republic of China
730 (NSTC-110-2113-M-001-064-MY3) and Academia Sinica, Taiwan (AS-CDA-108-L07).

731

732 **Author contributions**

733

734 **See-Khai Lim**: Conceptualization; Data curation; Formal analysis; Investigation; Methodology;
735 Writing—original draft; Writing—review and editing. **Wen-Ching Lin**: Data curation; Formal
736 analysis. **Yi-Chung Pan**: Data curation; Formal analysis. **Sin-Wei Huang**: Data curation. **Yao-An Yu**:
737 Data curation. **Cheng-Hung Cheng:** Data curation. **Che-Ming Jack Hu**: Formal analysis; Supervision;
738 Investigation; Writing—review and editing. **Chung-Yuan Mou**: Data curation; Supervision; Writing—
739 review and editing. **Kurt Yun Mou**: Conceptualization; Resources; Formal analysis; Supervision;
740 Funding acquisition; Validation; Methodology; Writing—original draft; Writing—review and editing.

741

742 **Acknowledgement**

743 The study is supported by the National Science and Technology Council of Taiwan (#110-2113-M-001-
744 064-MY3)

745

746 **Declaration of Interest**

747 S.-K. Lim and C.-M. J. Hu are listed as inventors on a patent application related to the present study.

748

749 **References**

750 1. Lim, S.K., et al., *Bacteria colonization in tumor microenvironment creates a favorable niche for*
751 *immunogenic chemotherapy.* EMBO Mol Med, 2024. **16**(2): p. 416-428.
752 2. Galluzzi, L., et al., *Targeting immunogenic cell stress and death for cancer therapy.* Nat Rev Drug
753 Discov, 2024. **23**(6): p. 445-460.
754 3. Waldman, A.D., J.M. Fritz, and M.J. Lenardo, *A guide to cancer immunotherapy: from T cell basic*
755 *science to clinical practice.* Nat Rev Immunol, 2020. **20**(11): p. 651-668.
756 4. Tan, S., D. Li, and X. Zhu, *Cancer immunotherapy: Pros, cons and beyond.* Biomed Pharmacother,
757 2020. **124**: p. 109821.
758 5. Taefehshokr, S., et al., *Cancer immunotherapy: Challenges and limitations.* Pathol Res Pract,
759 2022. **229**: p. 153723.
760 6. Park, J.H., et al., *Harnessing the Power of IL-7 to Boost T Cell Immunity in Experimental and*
761 *Clinical Immunotherapies.* Immune Netw, 2024. **24**(1): p. e9.
762 7. Fu, Y., R. Tang, and X. Zhao, *Engineering cytokines for cancer immunotherapy: a systematic*
763 *review.* Front Immunol, 2023. **14**: p. 1218082.
764 8. Waickman, A.T., J.Y. Park, and J.H. Park, *The common gamma-chain cytokine receptor: tricks-and-*
765 *treats for T cells.* Cell Mol Life Sci, 2016. **73**(2): p. 253-69.
766 9. Holcomb, E.A. and W. Zou, *A forced marriage of IL-2 and PD-1 antibody nurtures tumor-*
767 *infiltrating T cells.* J Clin Invest, 2022. **132**(3).
768 10. Shen, S., et al., *Engineered IL-21 Cytokine Muteins Fused to Anti-PD-1 Antibodies Can Improve*
769 *CD8+ T Cell Function and Anti-tumor Immunity.* Front Immunol, 2020. **11**: p. 832.
770 11. Silva, D.-A., et al., *De novo design of potent and selective mimics of IL-2 and IL-15.* Nature, 2019.
771 **565**(7738): p. 186-191.
772 12. Mizui, M., *Natural and modified IL-2 for the treatment of cancer and autoimmune diseases.* Clin
773 Immunol, 2019. **206**: p. 63-70.
774 13. Knudson, K.M., et al., *Rationale for IL-15 superagonists in cancer immunotherapy.* Expert Opin
775 Biol Ther, 2020. **20**(7): p. 705-709.
776 14. Steele, N., et al., *A phase 1 trial of recombinant human IL-21 in combination with cetuximab in*
777 *patients with metastatic colorectal cancer.* Br J Cancer, 2012. **106**(5): p. 793-8.
778 15. Portielje, J.E., et al., *Phase I study of subcutaneously administered recombinant human*
779 *interleukin 12 in patients with advanced renal cell cancer.* Clin Cancer Res, 1999. **5**(12): p. 3983-9.
780 16. Lin, J.X. and W.J. Leonard, *The Common Cytokine Receptor gamma Chain Family of Cytokines.*
781 Cold Spring Harb Perspect Biol, 2018. **10**(9).

782 17. Sim, G.C. and L. Radvanyi, *The IL-2 cytokine family in cancer immunotherapy.* Cytokine Growth
783 Factor Rev, 2014. **25**(4): p. 377-90.
784 18. Winer, H., et al., *IL-7: Comprehensive review.* Cytokine, 2022. **160**: p. 156049.
785 19. Lee, K.J., et al., *IL-7-primed bystander CD8 tumor-infiltrating lymphocytes optimize the antitumor*
786 *efficacy of T cell engager immunotherapy.* Cell Rep Med, 2024. **5**(5): p. 101567.
787 20. Kim, J.H., et al., *Hybrid Fc-fused interleukin-7 induces an inflamed tumor microenvironment and*
788 *improves the efficacy of cancer immunotherapy.* Clin Transl Immunology, 2020. **9**(9): p. e1168.
789 21. Tredan, O., et al., *ELYPSE-7: a randomized placebo-controlled phase IIa trial with CYT107*
790 *exploring the restoration of CD4+ lymphocyte count in lymphopenic metastatic breast cancer*
791 *patients.* Ann Oncol, 2018. **29**(2): p. 523.
792 22. Perales, M.A., et al., *Recombinant human interleukin-7 (CYT107) promotes T-cell recovery after*
793 *allogeneic stem cell transplantation.* Blood, 2012. **120**(24): p. 4882-91.
794 23. Sportes, C., et al., *Phase I study of recombinant human interleukin-7 administration in subjects*
795 *with refractory malignancy.* Clin Cancer Res, 2010. **16**(2): p. 727-35.
796 24. Fu, C., et al., *Advances in IL-7 Research on Tumour Therapy.* Pharmaceuticals (Basel), 2024. **17**(4).
797 25. McElroy, C.A., J.A. Dohm, and S.T. Walsh, *Structural and biophysical studies of the human IL-7/IL-*
798 *7Ralpha complex.* Structure, 2009. **17**(1): p. 54-65.
799 26. Kwon, D.I., et al., *Fc-fused IL-7 provides broad antiviral effects against respiratory virus infections*
800 *through IL-17A-producing pulmonary innate-like T cells.* Cell Rep Med, 2024. **5**(1): p. 101362.
801 27. Foss, S., et al., *Human IgG Fc-engineering for enhanced plasma half-life, mucosal distribution and*
802 *killing of cancer cells and bacteria.* Nature Communications, 2024. **15**(1): p. 2007.
803 28. Martin, C.E., et al., *IL-7/anti-IL-7 mAb complexes augment cytokine potency in mice through*
804 *association with IgG-Fc and by competition with IL-7R.* Blood, 2013. **121**(22): p. 4484-92.
805 29. Mausser, E., et al., *LALAPG variant of the Human Contraception Antibody (HCA) reduces Fc-*
806 *mediated effector functions while maintaining sperm agglutination activity.* PLoS One, 2023.
807 **18**(3): p. e0282147.
808 30. Sarkar, O.S., et al., *Monocytic MDSCs exhibit superior immune suppression via adenosine and*
809 *depletion of adenosine improves efficacy of immunotherapy.* Sci Adv, 2023. **9**(26): p. eadg3736.
810 31. Gallina, G., et al., *Tumors induce a subset of inflammatory monocytes with immunosuppressive*
811 *activity on CD8+ T cells.* J Clin Invest, 2006. **116**(10): p. 2777-90.
812 32. Ouyang, Y., et al., *Tumor-associated neutrophils suppress CD8(+) T cell immunity in urothelial*
813 *bladder carcinoma through the COX-2/PGE2/IDO1 Axis.* Br J Cancer, 2024. **130**(5): p. 880-891.

814 33. Xue, L., et al., *Coupling of the cell cycle and apoptotic machineries in developing T cells.* J Biol
815 Chem, 2010. **285**(10): p. 7556-65.
816 34. Eum, H.H., et al., *Single-cell RNA sequencing reveals myeloid and T cell co-stimulation mediated*
817 *by IL-7 anti-cancer immunotherapy.* Br J Cancer, 2024. **130**(8): p. 1388-1401.
818 35. Jacobs, S.R., R.D. Michalek, and J.C. Rathmell, *IL-7 is essential for homeostatic control of T cell*
819 *metabolism in vivo.* J Immunol, 2010. **184**(7): p. 3461-9.
820 36. Hope, H.C. and R.J. Salmond, *The Role of Non-essential Amino Acids in T Cell Function and Anti-*
821 *tumour Immunity.* Arch Immunol Ther Exp (Warsz), 2021. **69**(1): p. 29.
822 37. Han, C., et al., *Fueling T-cell Antitumor Immunity: Amino Acid Metabolism Revisited.* Cancer
823 Immunol Res, 2021. **9**(12): p. 1373-1382.
824 38. Shyer, J.A., R.A. Flavell, and W. Bailis, *Metabolic signaling in T cells.* Cell Research, 2020. **30**(8): p.
825 649-659.
826 39. Ma, E.H., et al., *Serine Is an Essential Metabolite for Effector T Cell Expansion.* Cell Metab, 2017.
827 **25**(2): p. 482.
828 40. Sugiura, A., et al., *MTHFD2 is a metabolic checkpoint controlling effector and regulatory T cell*
829 *fate and function.* Immunity, 2022. **55**(1): p. 65-81.e9.
830 41. Anderson, A.C., N. Joller, and V.K. Kuchroo, *Lag-3, Tim-3, and TIGIT: Co-inhibitory Receptors with*
831 *Specialized Functions in Immune Regulation.* Immunity, 2016. **44**(5): p. 989-1004.
832 42. Gumber, D. and L.D. Wang, *Improving CAR-T immunotherapy: Overcoming the challenges of T*
833 *cell exhaustion.* EBioMedicine, 2022. **77**: p. 103941.
834 43. Tang, A. and F. Harding, *The challenges and molecular approaches surrounding interleukin-2-*
835 *based therapeutics in cancer.* Cytokine: X, 2019. **1**(1): p. 100001.
836 44. Broom, A., et al., *Designed protein reveals structural determinants of extreme kinetic stability.*
837 Proc Natl Acad Sci U S A, 2015. **112**(47): p. 14605-10.
838 45. Celej, M.S., G.G. Montich, and G.D. Fidelio, *Protein stability induced by ligand binding correlates*
839 *with changes in protein flexibility.* Protein Sci, 2003. **12**(7): p. 1496-506.
840 46. Majewski, M., S. Ruiz-Carmona, and X. Barril, *An investigation of structural stability in protein-*
841 *ligand complexes reveals the balance between order and disorder.* Communications Chemistry,
842 2019. **2**(1): p. 110.
843 47. Huang, P.S., et al., *RosettaRemodel: a generalized framework for flexible backbone protein*
844 *design.* PLoS One, 2011. **6**(8): p. e24109.

845 48. Liu, J., et al., *Enhancing alphafold-multimer-based protein complex structure prediction with*
846 *MULTICOM in CASP15.* Commun Biol, 2023. **6**(1): p. 1140.
847 49. Jumper, J., et al., *Highly accurate protein structure prediction with AlphaFold.* Nature, 2021.
848 **596**(7873): p. 583-589.
849 50. Schrödinger, L., & DeLano, W. *PyMOL.* 2020; Available from: http://www.pymol.org/pymol.
850 51. Mirdita, M., et al., *ColabFold: making protein folding accessible to all.* Nat Methods, 2022. **19**(6):
851 p. 679-682.

852

853

854

855

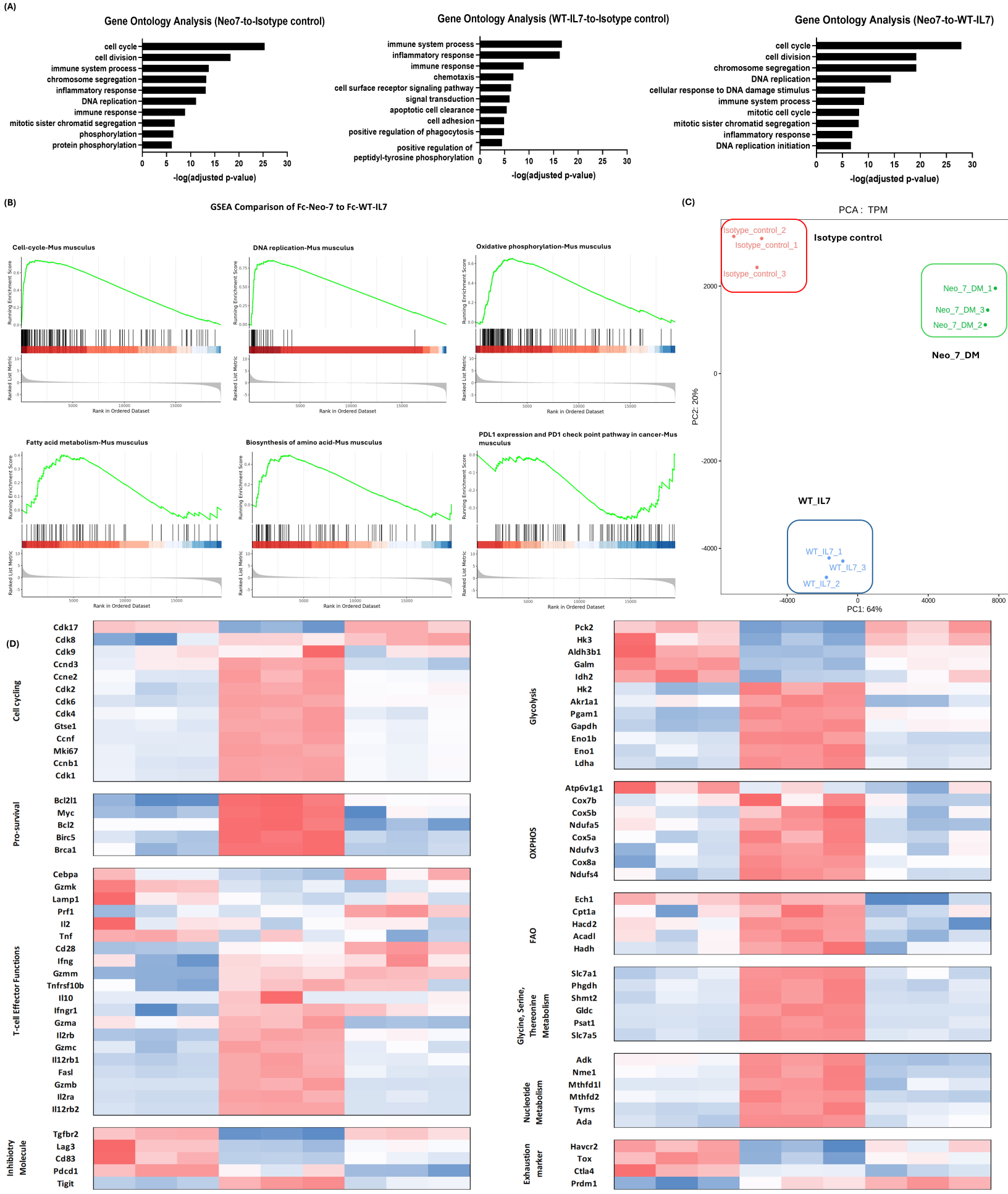
(A)
Gene Ontology Analysis (Neo7-to-Isotype control)
cell cycle
cell division
immune system process
chromosome segregation
inflammatory response
DNA replication
immune response
mitotic sister chromatid segregation
phosphorylation
protein phosphorylation
-log(adjusted p-value)
Gene Ontology Analysis (WT-IL7-to-Isotype control)
immune system process
inflammatory response
immune response
chemotaxis
cell surface receptor signaling pathway
signal transduction
apoptotic cell clearance
cell adhesion
positive regulation of phagocytosis
positive regulation of peptidyl-tyrosine phosphorylation
-log(adjusted p-value)
Gene Ontology Analysis (Neo7-to-WT-IL7)
cell cycle
cell division
chromosome segregation
DNA replication
cellular response to DNA damage stimulus
immune system process
mitotic cell cycle
mitotic sister chromatid segregation
inflammatory response
DNA replication initiation
-log(adjusted p-value)
(B)
GSEA Comparison of Fc-Neo-7 to Fc-WT-IL7
Cell-cycle-Mus musculus
DNA replication-Mus musculus
Oxidative phosphorylation-Mus musculus
Fatty acid metabolism-Mus musculus
Biosynthesis of amino acid-Mus musculus
PDL1 expression and PD1 check point pathway in cancer-Mus musculus
Running Enrichment Score
Ranked List Metric
Rank in Ordered Dataset
(C)
PCA : TPM
Isotype_control_2
Isotype_control_1
Isotype_control_3
Isotype control
Neo_7_DM_1
Neo_7_DM_3
Neo_7_DM_2
Neo_7_DM
WT_IL7
WT_IL7_1
WT_IL7_3
WT_IL7_2
PC2: 20%
PC1: 64%
(D)
Cell cycling
Cdk17
Cdk8
Cdk9
Ccnd3
Ccne2
Cdk2
Cdk6
Cdk4
Gtse1
Ccnf
Mki67
Ccnb1
Cdk1
Pro-survival
Bcl2l1
Myc
Bcl2
Birc5
Brca1
T-cell Effector Functions
Cebpa
Gzmk
Lamp1
Prf1
Il2
Tnf
Cd28
Ifng
Gzmm
Tnfrsf10b
Il10
Ifngr1
Gzma
Il2rb
Gzmc
Il12rb1
Fasl
Gzmb
Il2ra
Il12rb2
Inhibiotry Molecule
Tgfbr2
Lag3
Cd83
Pdcd1
Tigit
Glycolysis
Pck2
Hk3
Aldh3b1
Galm
Idh2
Hk2
Akr1a1
Pgam1
Gapdh
Eno1b
Eno1
Ldha
OXPHOS
Atp6v1g1
Cox7b
Cox5b
Ndufa5
Cox5a
Ndufv3
Cox8a
Ndufs4
FAO
Ech1
Cpt1a
Hacd2
Acadl
Hadh
Glycine, Serine, Thereonine Metabolism
Slc7a1
Phgdh
Shmt2
Gldc
Psat1
Slc7a5
Nucleotide Metabolism
Adk
Nme1
Mthfd1l
Mthfd2
Tyms
Ada
Exhaustion marker
Havcr2
Tox
Ctla4
Prdm1

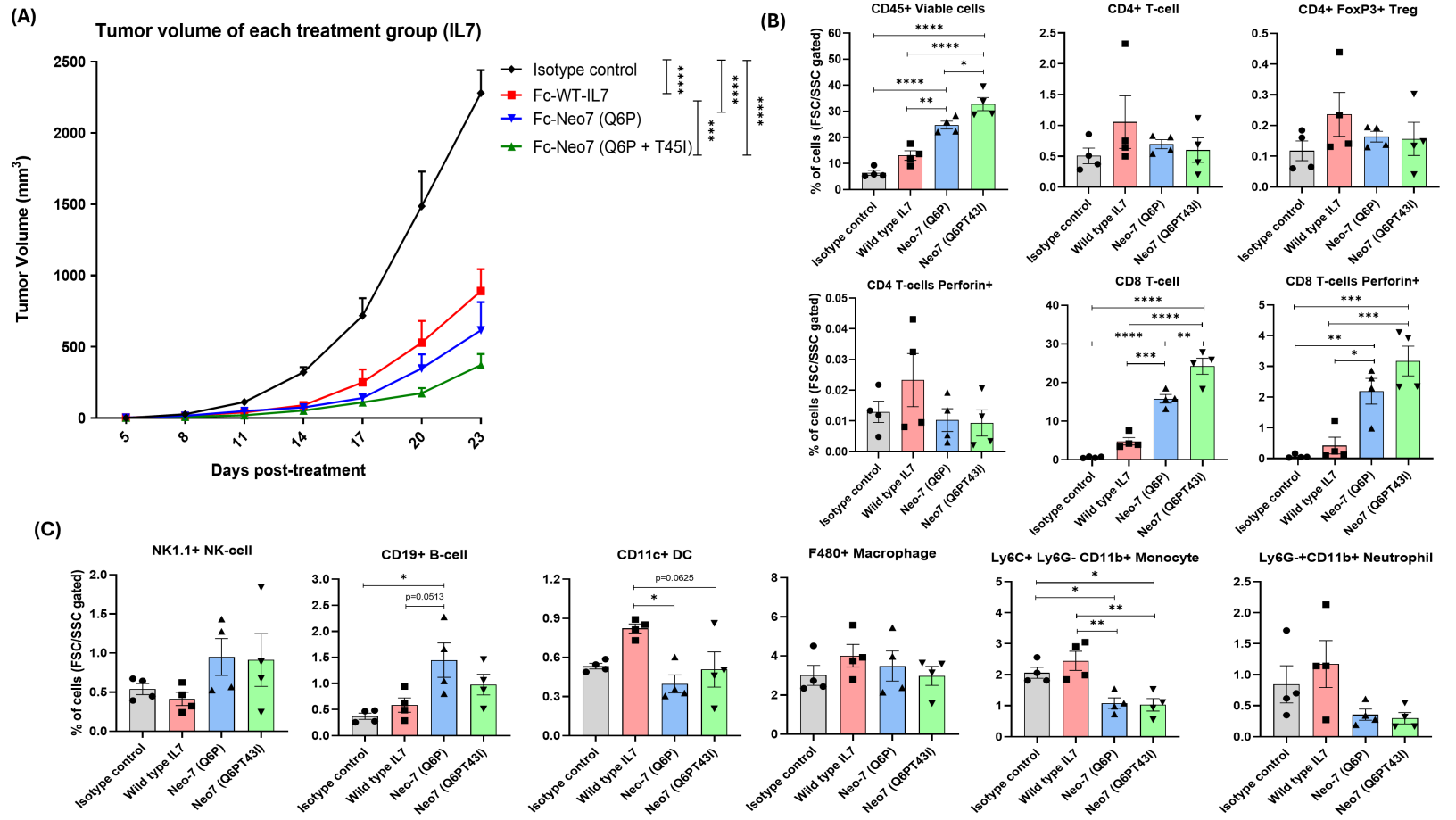
(A)
Tumor volume of each treatment group (IL7)
Tumor Volume (mm3)
Days post-treatment
Isotype control
Fc-WT-IL7
Fc-Neo7 (Q6P)
Fc-Neo7 (Q6P + T45I)
(B)
CD45+ Viable cells
CD4+ T-cell
CD4+ FoxP3+ Treg
CD4 T-cells Perforin+
CD8 T-cell
CD8 T-cells Perforin+
% of cells (FSC/SSC gated)
Isotype control
Wild type IL7
Neo-7 (Q6P)
Neo7 (Q6PT43I)
(C)
NK1.1+ NK-cell
CD19+ B-cell
CD11c+ DC
F480+ Macrophage
Ly6C+ Ly6G- CD11b+ Monocyte
Ly6G-+CD11b+ Neutrophil
p=0.0513
p=0.0625

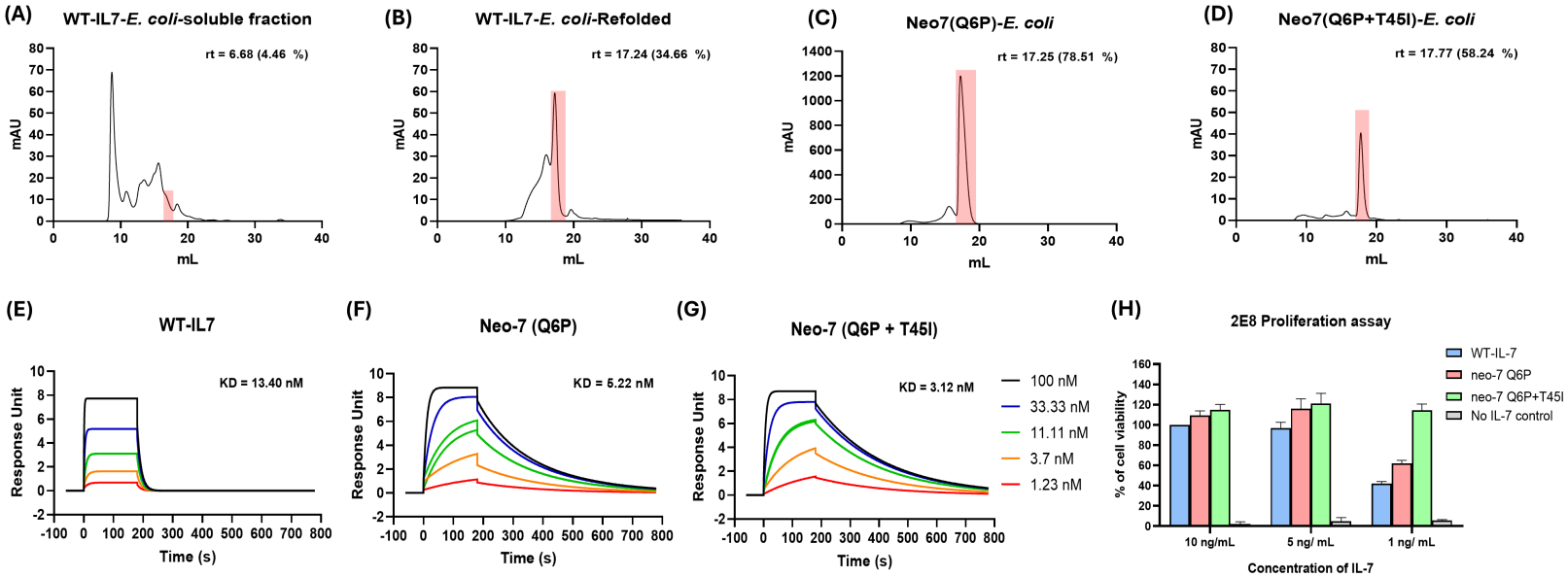
(A)
WT-IL7-E. coli-soluble fraction
rt = 6.68 (4.46 %)
mAU
mL
(B)
WT-IL7-E. coli-Refolded
rt = 17.24 (34.66 %)
mAU
mL
(C)
Neo7(Q6P)-E. coli
rt = 17.25 (78.51 %)
mAU
mL
(D)
Neo7(Q6P+T45I)-E. coli
rt = 17.77 (58.24 %)
mAU
mL
(E)
WT-IL7
KD = 13.40 nM
Response Unit
Time (s)
(F)
Neo-7 (Q6P)
KD = 5.22 nM
Response Unit
Time (s)
(G)
Neo-7 (Q6P + T45I)
KD = 3.12 nM
100 nM
33.33 nM
11.11 nM
3.7 nM
1.23 nM
Response Unit
Time (s)
(H)
2E8 Proliferation assay
WT-IL-7
neo-7 Q6P
neo-7 Q6P+T45I
No IL-7 control
% of cell viability
10 ng/mL
5 ng/ mL
1 ng/ mL
Concentration of IL-7

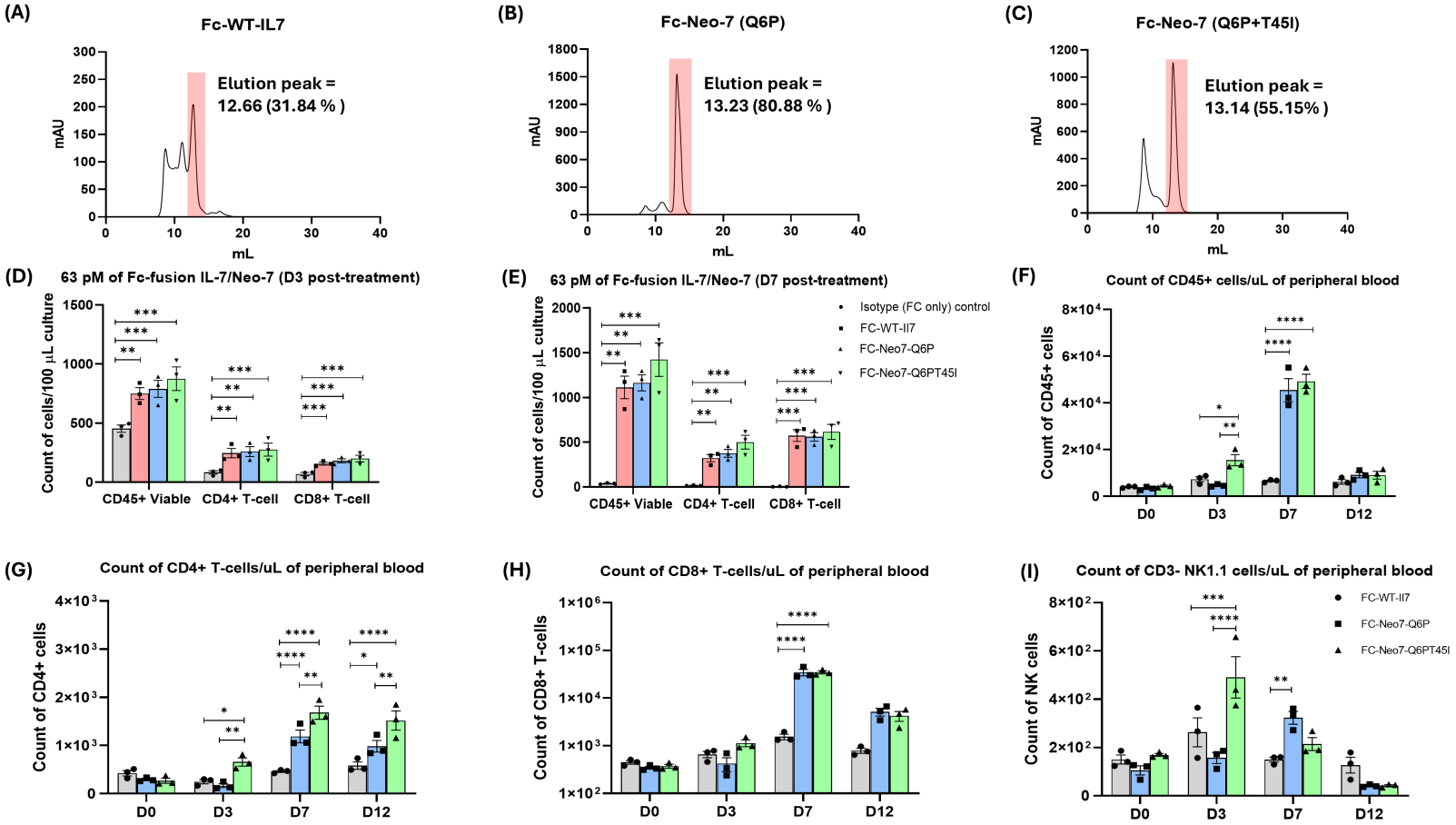
(A)
Fc-WT-IL7
Elution peak =
12.66 (31.84 %)
mAU
mL
(B)
Fc-Neo-7 (Q6P)
Elution peak =
13.23 (80.88 %)
mAU
mL
(C)
Fc-Neo-7 (Q6P+T45I)
Elution peak =
13.14 (55.15%)
mAU
mL
(D)
63 pM of Fc-fusion IL-7/Neo-7 (D3 post-treatment)
Count of cells/100 μL culture
CD45+ Viable
CD4+ T-cell
CD8+ T-cell
(E)
63 pM of Fc-fusion IL-7/Neo-7 (D7 post-treatment)
Count of cells/100 μL culture
CD45+ Viable
CD4+ T-cell
CD8+ T-cell
Isotype (FC only) control
FC-WT-Il7
FC-Neo7-Q6P
FC-Neo7-Q6PT45I
(F)
Count of CD45+ cells/uL of peripheral blood
Count of CD45+ cells
D0
D3
D7
D12
(G)
Count of CD4+ T-cells/uL of peripheral blood
Count of CD4+ cells
D0
D3
D7
D12
(H)
Count of CD8+ T-cells/uL of peripheral blood
Count of CD8+ T-cells
D0
D3
D7
D12
(I)
Count of CD3- NK1.1 cells/uL of peripheral blood
Count of NK cells
FC-WT-Il7
FC-Neo7-Q6P
FC-Neo7-Q6PT45I
D0
D3
D7
D12

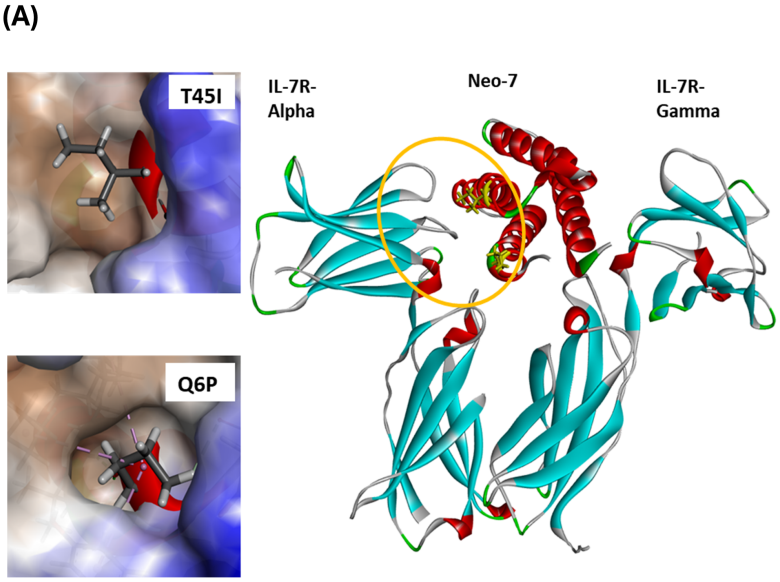
(A)
T45I
Q6P
IL-7R-
Alpha
Neo-7
IL-7R-
Gamma

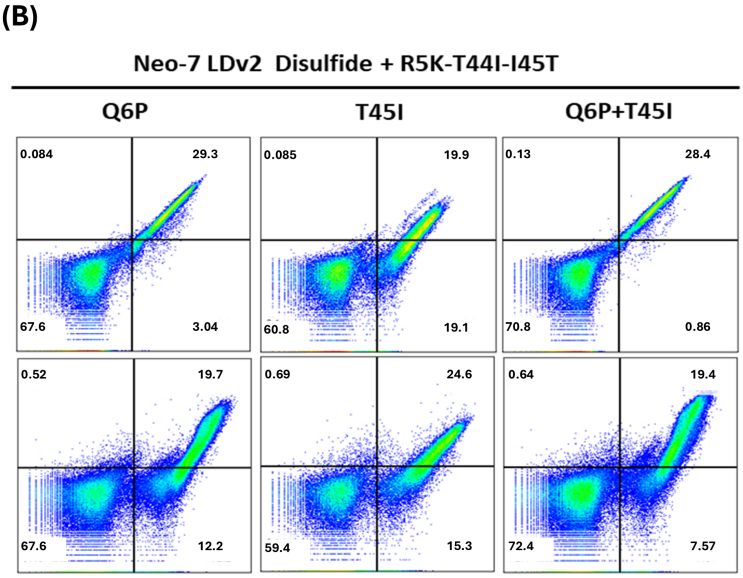
(B)
Neo-7 LDv2 Disulfide + R5K-T44I-I45T
Q6P
T45I
Q6P+T45I
0.084
29.3
67.6
3.04
0.085
19.9
60.8
19.1
0.13
28.4
70.8
0.86
0.52
19.7
67.6
12.2
0.69
24.6
59.4
15.3
0.64
19.4
72.4
7.57

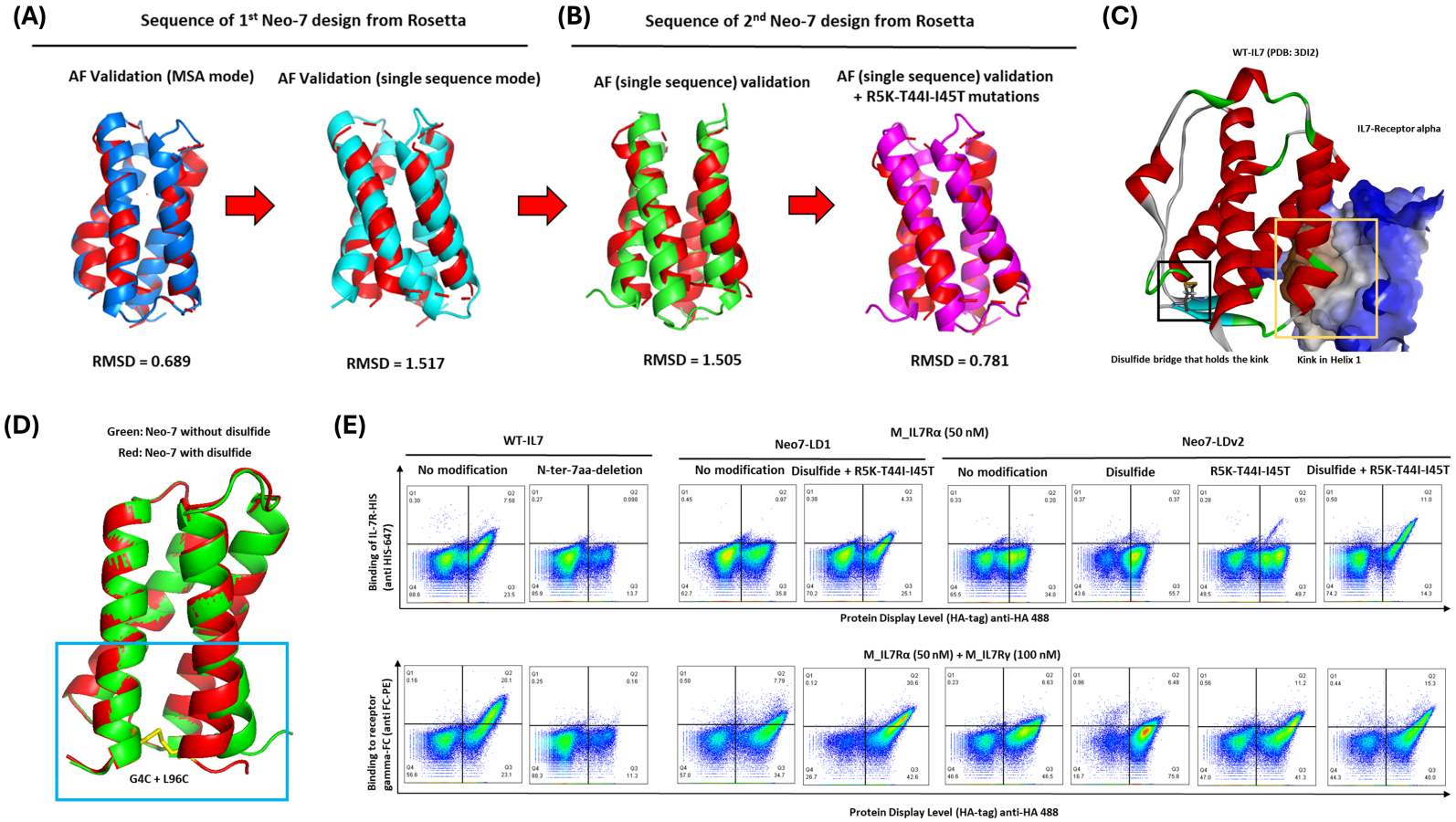
(A)
Sequence of 1st Neo-7 design from Rosetta
AF Validation (MSA mode)
AF Validation (single sequence mode)
RMSD = 0.689
RMSD = 1.517
(B)
Sequence of 2nd Neo-7 design from Rosetta
AF (single sequence) validation
AF (single sequence) validation
+ R5K-T44I-I45T mutations
RMSD = 1.505
RMSD = 0.781
(C)
WT-IL7 (PDB: 3DI2)
IL7-Receptor alpha
Disulfide bridge that holds the kink
Kink in Helix 1
(D)
Green: Neo-7 without disulfide
Red: Neo-7 with disulfide
G4C + L96C
(E)
WT-IL7
Neo7-LD1
M_IL7Rα (50 nM)
Neo7-LDv2
No modification
N-ter-7aa-deletion
No modification
Disulfide + R5K-T44I-I45T
No modification
Disulfide
R5K-T44I-I45T
Disulfide + R5K-T44I-I45T
Binding of IL-7R-HIS (anti HIS-647)
Protein Display Level (HA-tag) anti-HA 488
M_IL7Rα (50 nM) + M_IL7Rγ (100 nM)
Binding to receptor gamma-FC (anti FC-PE)
Protein Display Level (HA-tag) anti-HA 488

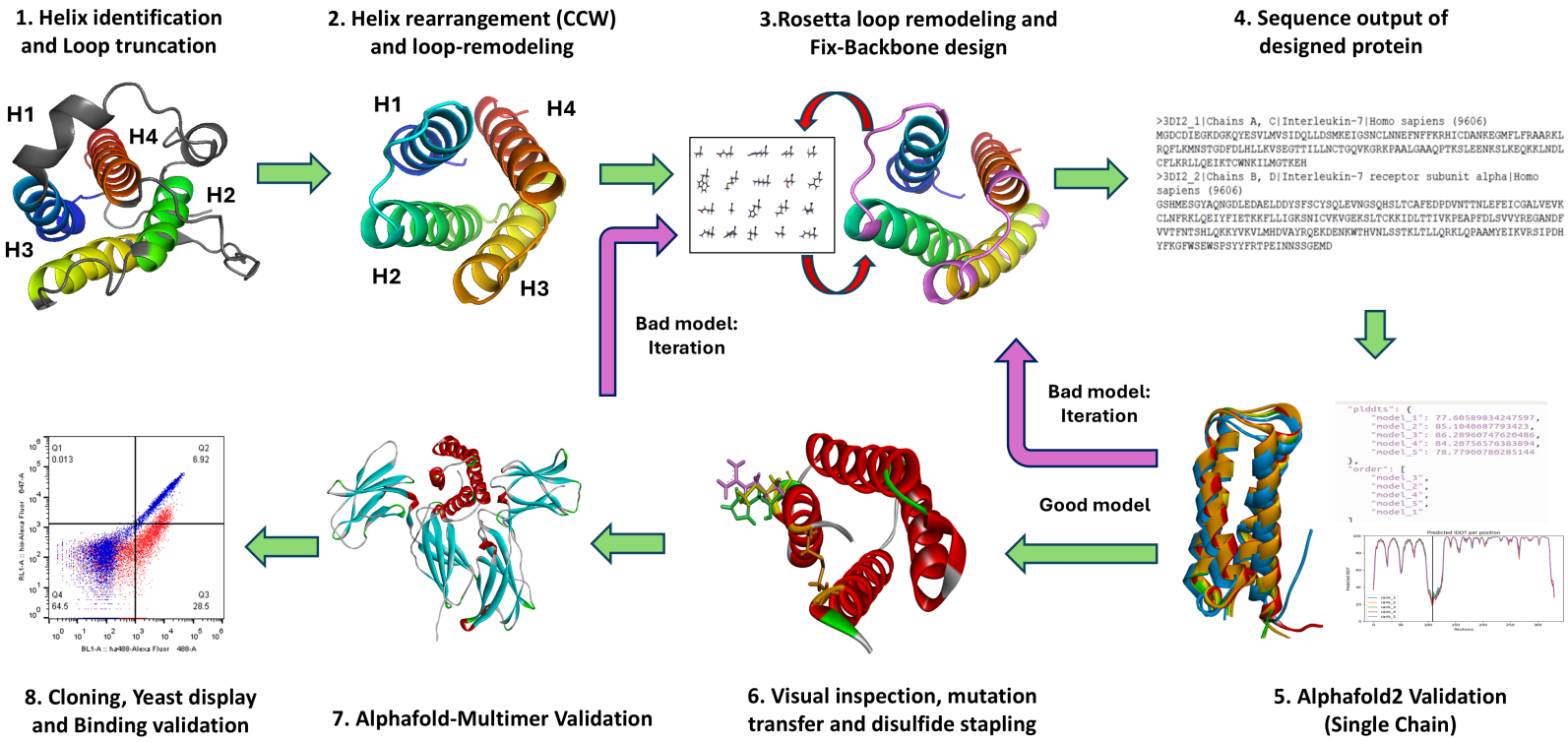
1. Helix identification and Loop truncation
H1
H4
H2
H3
2. Helix rearrangement (CCW) and loop-remodeling
H1
H4
H2
H3
3.Rosetta loop remodeling and Fix-Backbone design
Bad model: Iteration
4. Sequence output of designed protein
>3DI2_1|Chains A, C|Interleukin-7|Homo sapiens (9606)
MGDCDIEGKDGKQYESVLMVSIDQLLDSMKEIGSNCLNNEFNFFKRHICDANKEGMFLFRAARKL
RQFLKMNSTGDFDLHLLKVSEGTTILLNCTGQVKGRKPAALGAAQPTKSLEENKSLKEQKKLNDL
CFLKRLLQEIKTCWNKILMGTKEH
>3DI2_2|Chains B, D|Interleukin-7 receptor subunit alpha|Homo sapiens (9606)
GSHMESGYAQNGDLEDAELDDYSFSCYSQLEVNGSQHSLTCAFEDPDVNTTNLEFEICGALVEVK
CLNFRKLQEIYFIETKKFLLIGKSNICVKVGEKSLTCKKIDLTTIVKPEAPFDLSVVYREGANDF
VVTFNTSHLQKKYVKVLMHDVAYRQEKDENKWTHVNLSSTKLTLLQRKLQPAAMYEIKVRSIPDH
YFKGFWSEWSPSYYFRTPEINNSSGEMD
Bad model: Iteration
Good model
"plddts": {
"model_1": 77.60589834247597,
"model_2": 85.10400687793423,
"model_3": 86.28960747620486,
"model_4": 84.20756576383894,
"model_5": 78.77900780285144
},
"order": [
"model_3",
"model_2",
"model_4",
"model_5",
"model_1"
]
Predicted IDDT per position
Q1 0.013
Q2 6.92
Q4 64.5
Q3 28.5
8. Cloning, Yeast display and Binding validation
7. Alphafold-Multimer Validation
6. Visual inspection, mutation transfer and disulfide stapling
5. Alphafold2 Validation (Single Chain)

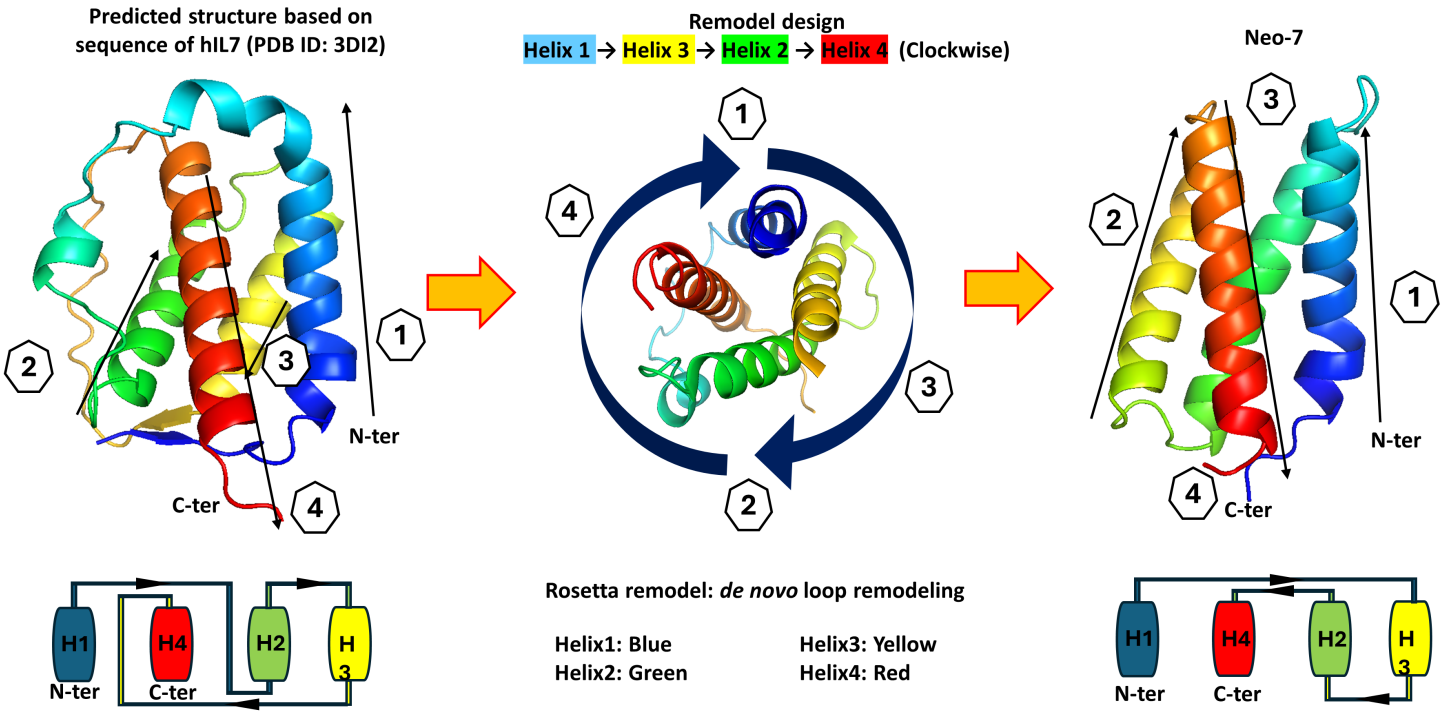
Predicted structure based on sequence of hIL7 (PDB ID: 3DI2)
Remodel design
Helix 1 → Helix 3 → Helix 2 → Helix 4 (Clockwise)
Neo-7
1
2
3
4
N-ter
C-ter
H1
H4
H2
H 3
Rosetta remodel: *de novo* loop remodeling
Helix1: Blue
Helix2: Green
Helix3: Yellow
Helix4: Red